CrossMark

Starspot Mapping with Adaptive Parallel Tempering. II. Application to TESS Data for M-dwarf Flare Stars AU Microscopii, YZ Canis Minoris, and EV Lacertae

Kai Ikuta[1,12] , Kosuke Namekata[2] , Yuta Notsu[3,4,5] , Hiroyuki Maehara[1,6] , Soshi Okamoto[7,8] , Satoshi Honda[9] ,
Daisaku Nogami[7] , and Kazunari Shibata[10,11]

[1] Astronomical Observatory, Kyoto University, Kitashirakawa-Oiwake-cho, Sakyo, Kyoto 606–8502, Japan; ikuta@kusastro.kyoto-u.ac.jp
[2] ALMA Project, National Astronomical Observatory of Japan, NINS, Mitaka, Tokyo 181–8588, Japan
[3] Laboratory for Atmospheric and Space Physics, University of Colorado Boulder, 3665 Discovery Drive, Boulder, Colorado 80303, USA
[4] National Solar Observatory, 3665 Discovery Drive, Boulder, Colorado 80303, USA
[5] Department of Earth and Planetary Sciences, Tokyo Institute of Technology, 2-12-1 Ookayama, Meguro, Tokyo 152–8551, Japan
[6] Okayama Branch Office, Subaru Telescope, National Astronomical Observatory of Japan, NINS, Kamogata, Asakuchi, Okayama 719–0232, Japan
[7] Department of Astronomy, Kyoto University, Kitashirakawa-Oiwake-cho, Sakyo, Kyoto 606–8502, Japan
[8] Japan Meteorological Agency, 1-3-4 Otemachi, Chiyoda, Tokyo 100-8122, Japan
[9] Nishi-Harima Astronomical Observatory, University of Hyogo, 407-2 Nishigaichi, Sayo-cho, Sayo, Hyogo 679–5313, Japan
[10] Kwasan Observatory, Kyoto University, 17 Ohmine-cho, Kita-Kazan, Yamashina, Kyoto 607–8471, Japan
[11] Department of Environmental Systems Science, Doshisha University, 1-3 Tataramiyakodani, Kyotanabe, Kyoto 610–0394, Japan

Abstract

Starspots and stellar flares are indicators of stellar magnetic activity. The magnetic energy stored around spots is thought to be the origin of flares, but the connection is not completely understood. To investigate the relation between spot locations deduced from light curves and the occurrence of flares therein, we perform starspot modeling for the TESS light curves of three M-dwarf flare stars, AU Mic, YZ CMi, and EV Lac, using the code implemented in Paper I. The code enables us to deduce multiple stellar/spot parameters by the adaptive parallel tempering algorithm efficiently. We find that flare occurrence frequency is not necessarily correlated with the rotation phases of the light curve for each star. The result of starspot modeling shows that any spot is always visible to the line of sight in all phases, and we suggest that this can be one of the reasons why there is no or low correlation between rotation phases and flare frequency. In addition, the amplitude and shape of the light curve for AU Mic and YZ CMi have varied in two years between different TESS cycles. The result of starspot modeling suggests that this can be explained by the variations of spot size and latitude.

Unified Astronomy Thesaurus concepts: Starspots (1572); Stellar flares (1603); M dwarf stars (982); Markov chain Monte Carlo (1889); Importance sampling (1892); Model selection (1912); Astrostatistics (1882)

1. Introduction

Starspots are apparent manifestations of magnetic activity on the stellar surface, and can be ubiquitously observed on various types of stars (for reviews, see Berdyugina 2005; Strassmeier 2009; Kochukhov 2021). For active young stars, cool stars (M-, K-, and G-dwarfs), and RS CVn–type stars, starspots have been extensively studied through ground-based observations of photometry (e.g., Henry et al. 1995; Messina & Guinan 2002) and spectroscopy (e.g., Strassmeier & Bopp 1992; Strassmeier et al. 1999). Stellar flares are intense explosions in the stellar atmosphere by the release of magnetic energy around starspots, and they have extensively been studied in close association with spots (e.g., Pettersen 1980; Hawley & Pettersen 1991; Gershberg 2005; Benz & Güdel 2010). In particular, starspot and stellar flare studies have been enabled with high precision and long-term photometry by the advent of the Kepler Space Telescope (Koch et al. 2010) and the Transiting Exoplanet Survey Satellite (TESS; Ricker et al. 2015). Many superflares have been reported on a large number of cool stars for Kepler

data (Maehara et al. 2012; Davenport et al. 2014; Hawley et al. 2014; Karoff et al. 2016; Notsu et al. 2019; Okamoto et al. 2021) and TESS data (e.g., Feinstein et al. 2020; Günther et al. 2020; Tu et al. 2020, 2021; Namekata et al. 2021, 2022). The spot size estimated from the amplitude of the light curve is determined by the upper limit of the flare energy for Kepler data of solar-type stars, and stars with larger spots cause larger flares as in the case of solar flares (Notsu et al. 2013; Shibata et al. 2013; Maehara et al. 2017; Okamoto et al. 2021). Hawley et al. (2014) and Silverberg et al. (2016) investigated the relation between the rotation phase of Kepler light curves and the occurrence of flares therein for an active dMe star GJ 1243 and found that the rotation phase and flare frequency are not correlated. They suggested that this could be because there are large spots on the visible pole or small spots are distributed in the whole stellar disk. Ensemble studies also suggest that the flare frequency is not necessarily correlated with the phase of the light curve for Kepler/K2 data (e.g., Doyle et al. 2018) and TESS data (Doyle et al. 2020; Feinstein et al. 2020).

It is unknown where the spots are actually on the stellar surface because the surface cannot be spatially resolved with a simple analysis from the light curve. Therefore, it is important to investigate the relation between the spot locations and flare occurrence by mapping the surface with sophisticated analysis, hereafter referred to as starspot modeling. Davenport et al. (2015) conducted starspot modeling for the Kepler light curve of GJ 1243 with a two-spot model and showed that the

---

[12] Current affiliation: Department of Multidisciplinary Sciences, The University of Tokyo, 3-8-1 Komaba, Meguro, Tokyo 153–8902, Japan.

light curve can be explained by a spot on the stellar equator and another spot at a high latitude. Their starspot modeling supports the suggestion by Hawley et al. (2014) that flare frequency is not correlated with the spot location because of an always visible large spot on the pole. This kind of sophisticated analysis can be important to understanding the origin of flares, but only a small number of stars including GJ 1243 have been investigated from this point. Then, it is also necessary to model more light curves to understand the relation between spot locations and flare frequency on flare stars.

AU Microscopii (AU Mic), YZ Canis Minoris (YZ CMi), and EV Lacertae (EV Lac) are bright and magnetically active M-dwarf stars. These have been observed to monitor their flares and to investigate their spots by (Zeeman) Doppler imaging through ground-based observations. Recently, these targets have been spectroscopically observed at the same time as the TESS observations were made to delve into the flare mechanisms (e.g., Maehara et al. 2021). The spot locations can be one of the indicators of where flares occur on the stellar disk and which direction the plasma associated with the flares erupts to (Namekata et al. 2021). AU Mic is a young dM1e dwarf with a spatially resolved debris disk (Kalas et al. 2004), and it has been revealed to be a young planetary system harboring two warm Neptunes (Martioli et al. 2020; Plavchan et al. 2020; Gilbert et al. 2022) from a transit search (Hebb et al. 2007). Since AU Mic is magnetically active and frequently causes large flares (Kunkel 1970), it has been spectroscopically observed from radio (Kundu et al. 1987) to X-ray (Mitra-Kraev et al. 2005) wavelengths. Its surface is largely filled with strong magnetic fields (Klein et al. 2021, 2022), and the light curve exhibits rotational periodic modulations ascribed to starspots on the surface (Torres et al. 1972; Rodono et al. 1986; Butler et al. 1987; Plavchan et al. 2020). YZ CMi is a magnetically active dM4.5e dwarf. Flares are reported from radio (Spangler et al. 1974) through optical (Lacy et al. 1976) to X-ray (Grindlay & Heise 1975) wavelengths, and it has been spectroscopically observed for the flare properties (Kowalski et al. 2010; Maehara et al. 2021). The modulation of its light curve has been reported through ground-based observations (Pettersen et al. 1983; Zboril 2003). There are spots on the pole according to Zeeman Doppler imaging (Morin et al. 2008). EV Lac is a magnetically active dM3.5e dwarf that has been investigated for its flare properties (Osten et al. 2005; Honda et al. 2018; Muheki et al. 2020; Paudel et al. 2021). The modulation of its light curve has been reported through ground-based observations (Pettersen 1980; Pettersen et al. 1983), and there are also spots on the pole according to (Zeeman) Doppler imaging (Morin et al. 2008; Jeffers et al. 2022).

In this study, for the purpose of investigating spot properties and their relation to flare occurrences, we conduct starspot modeling for the TESS light curves of M-dwarf flare stars, AU Mic, YZ CMi, and EV Lac, using the code implemented in Ikuta et al. (2020, hereafter referred to as Paper I). In Paper I, the code was implemented for starspot modeling with an adaptive parallel tempering (PT) algorithm (e.g., Hukushima 1999; Vousden et al. 2016) and an importance sampling algorithm to deduce stellar/spot parameters specified in `macula` (Kipping 2012) and compare the number of spots in the Bayesian framework. This paper is organized as follows. In Section 2, we describe the TESS data, the flare detection, the calculation of flare energy, and the numerical setup for starspot

modeling of the data. In Section 3, we discuss the results of starspot modeling in terms of comparison with previous studies by photometry and spectroscopy, the relation between spot locations and flare frequency, the variation of the amplitude and shape of the light curve for AU Mic and YZ CMi in two years, and comparison of the number of spots in the Bayesian framework in addition to confirming the validity of starspot modeling. In Section 4, we conclude this paper and describe future prospects. In Appendix A, we describe the result with different assumptions for the light curve of EV Lac Cycle 2 to evaluate the uncertainties of the parameters. In Appendix B, we exhibit supplementary figures delineating the joint posterior distribution for each of the models.

2. Method

2.1. Preprocessing TESS Data and Flare Detection

AU Mic (TIC 441420236), YZ CMi (TIC 266744225), and EV Lac (TIC 154101678) were observed with 2 minute cadence by TESS in Sectors 1 (July 25 to August 22 in 2018), 7 (January 7 to February 2 in 2019), and 16 (September 11 to October 7 in 2019) through the TESS prime mission (Cycles 1 and 2), respectively. After that, AU Mic and YZ CMi were also observed in Sectors 27 (July 4 to 30 in 2020) and 34 (January 13 to February 9 in 2021) through the TESS extended mission (Cycle 3), respectively. We retrieve the PDC-SAP (Pre-search Data Conditioning Simple Aperture Photometry) flux from the MAST (Mikulski Archive for Space Telescopes) Portal website.[13] To confirm effects by TESS systematics due to scattered light and spacecraft drift, we derive the rotation period from the SAP light curves using the TESS systematics-insensitive periodograms (Hedges et al. 2020). As a result, we obtain periods of 4.872, 4.825, 2.778, 2.778, and 4.364 days for AU Mic Cycles 1 and 3, YZ CMi Cycles 1 and 3, and EV Lac Cycle 2, respectively. These values are consistent with the results deduced from the PDC-SAP light curves, and the detrended light curves correspond to the PDC-SAP light curves. Thus, we adopt the PDC-SAP light curves for the starspot modeling. For the case of EV Lac Cycle 2 as an example, we exhibit the result by a two-spot model with a systematic noise model by a Gaussian process (GP; Appendix A.3).

Figure 1 exhibits the TESS light curves in terms of the relative flux (black), the PDC-SAP flux normalized by its average excluding missing values. The vertical lines in each panel also represent the detected flares at each time (red) as per the following procedure. First, we detect flare candidates in the light curves by using `stella` (Feinstein et al. 2020). The code detects flares from TESS light curves with convolutional neural networks, and we adopt their pretrained model with the detected flares in Günther et al. (2020). Then, we adopt a flare probability of 0.1 and an amplitude of 10^{-3} for all trained 100 models to obtain as few false negatives as possible. We confirm the flare candidates as flares by eye because many false positives are included in the detected candidates (Feinstein et al. 2022). Second, after extracting confirmed flares from the light curves, we also extract outliers of modulations ascribed to spots from the remaining light curves with a Bessel filter (Maehara et al. 2021). Although a small number of outliers remain in the light curves, they do not affect the result of the
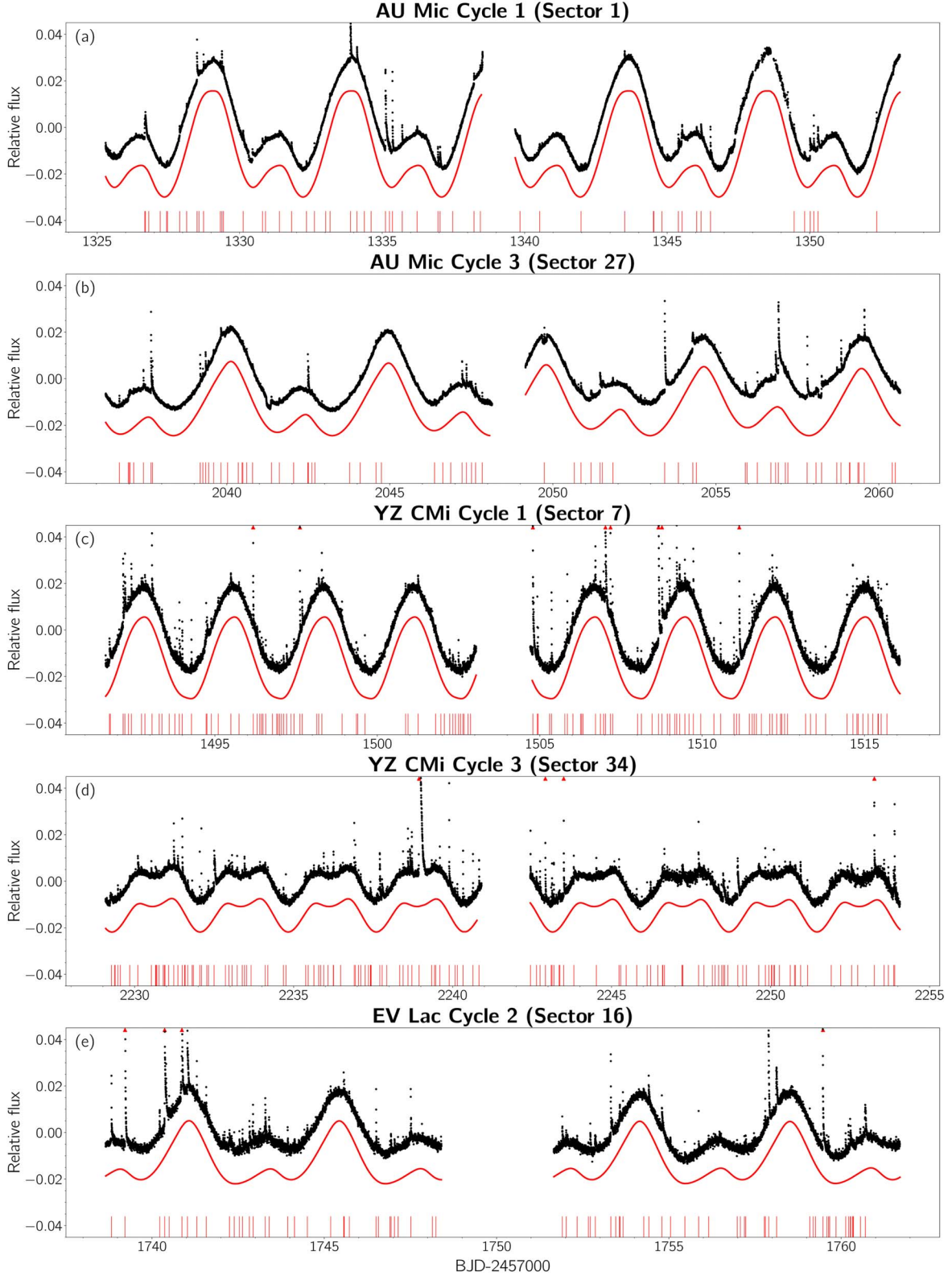

Figure 1. (a)–(e) TESS light curves of AU Mic Cycles 1 (Sector 1, July 25 to August 22 in 2018) and 3 (Sector 27, July 4 to 30 in 2020), YZ CMi Cycles 1 (Sector 7, January 7 to February 2 in 2019) and 3 (Sector 34, January 13 to February 9), and EV Lac Cycle 2 (Sector 16, September 11 to October 7 in 2019; black), respectively. The relative flux is calculated by the PDC-SAP flux normalized by its average excluding missing values. Detected flares are represented at each peak time (red bars; for details, see Section 2.1), and large flares are marked as outliers (red triangles). The reproduced light curves with two-spot models are also exhibited under the TESS light curves (red).

starspot modeling since the number of data points is much lower than the total number of data points. In this study, since the modulation timescale ascribed to spots is much longer than the cadence, we use data every three points for computational efficiency. As a result of the flare detection, the number of detected flares is summed up to 55, 70, 124, 137, and 76 for
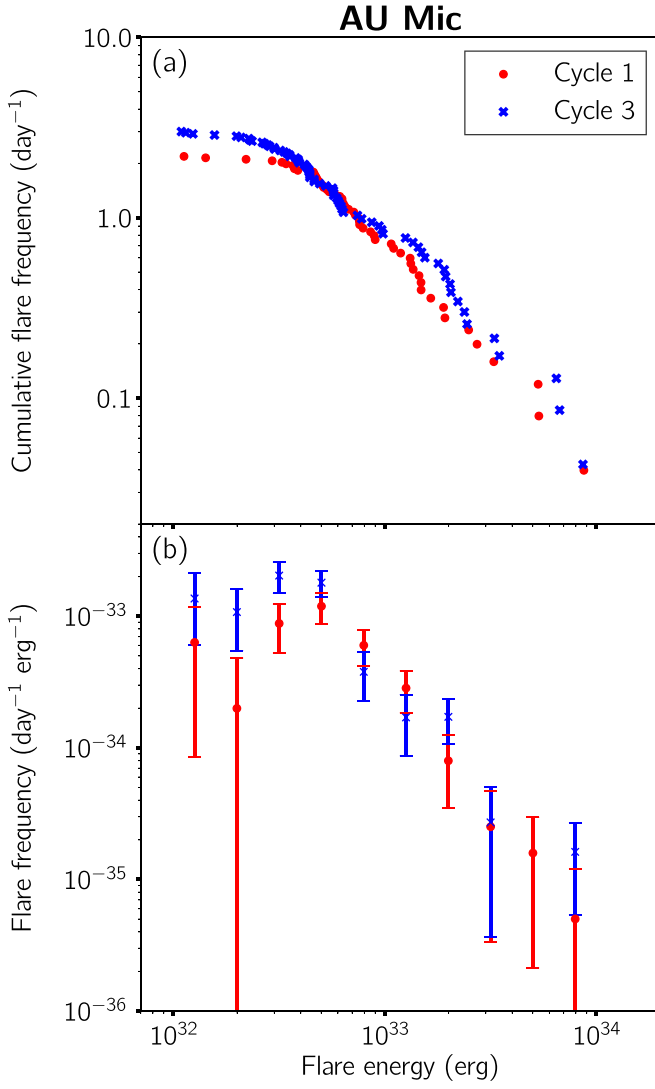
Figure 2. Flare frequency for AU Mic Cycles 1 (red) and 3 (blue). The number of flares per observation period of a TESS sector (Sectors 1 and 27) is 55/25.131 = 2.189 and 70/23.307 = 3.003 (day^{-1}), respectively. (a) Cumulative flare frequency distribution vs. bolometric flare energy: the number of flares per day with an energy higher than the energy value. (b) Flare frequency distribution vs. bolometric flare energy: the number of flares per day and the energy in each energy bin. The error bar equals the square root of (the number of flares in each energy bin + 1) per observation period and energy in each energy bin.

AU Mic Cycles 1 and 3, YZ CMi Cycles 1 and 3, and EV Lac Cycle 2, respectively (Figure 1).[14] The detectability of flares may depend on the rotation phase of the light curve because the amplitude of the light curve for these stars is large, and flares in the training set of the pretrained model are detected by reducing the periodic signal of the light curve (Günther et al. 2020). Thus, we consider the equivalent duration = 1 (s) as the sufficient threshold to discuss the correlation between spot locations and flare frequency. Among the detected flares, the number of flares with larger equivalent duration than 1 (s) is 48, 50, 109, 106, and 71, respectively.

---

[14] The flare properties are listed on GitHub (https://github.com/KaiIkuta/StarspotMapping) with a copy deposited to Zenodo (doi:10.5281/zenodo.7651850): the peak time (BJD-2,745,000), amplitude, equivalent duration (s), and e-folding time (day).
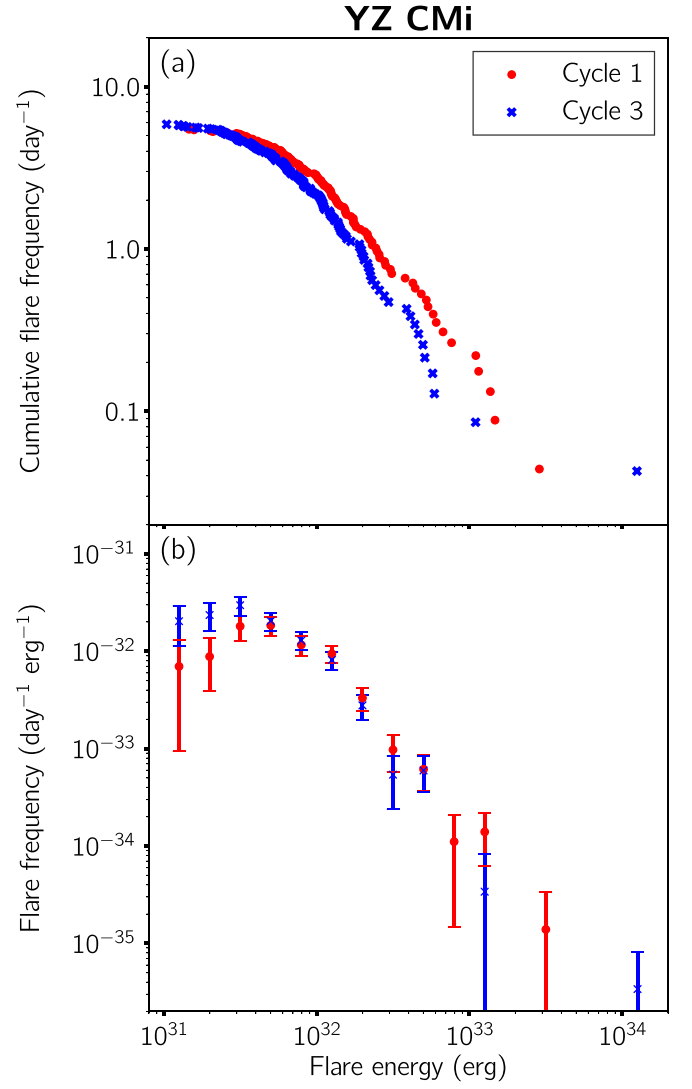
Figure 3. Same as Figure 2 but for YZ CMi Cycles 1 and 3. The number of flares per observation period of a TESS sector (Sectors 7 and 34) is 124/22.725 = 5.457 and 137/23.398 = 5.855 (day^{-1}), respectively.

According to Shibayama et al. (2013), the bolometric flare energy is formulated as

$$E_{\text{flare}} = \int L_{\text{flare}}(t)\,dt = \sigma_{\text{SB}} T_{\text{flare}}^4 \times 2\pi R_{\text{star}}^2$$

$$\times \frac{\int R(\lambda)B(\lambda, T_{\text{eff}})\,d\lambda}{\int R(\lambda)B(\lambda, T_{\text{flare}})\,d\lambda} \times \int \frac{\Delta F}{F}(t)\,dt, \qquad (1)$$

where $L_{\text{flare}}(t)$ and $\Delta F/F(t)$ are the bolometric luminosity and relative flux at time t, and $\sigma_{\text{SB}} = 5.67 \times 10^{-1}$ (erg K^{-4} m^{-2} s^{-1}) is the Stefan–Boltzmann constant. The flare is assumed to be blackbody radiation with a flare temperature $T_{\text{flare}} = 10{,}000$ (K). The last time-integrated factor corresponds to the equivalent duration, which is calculated by the integral of the relative flux with time from the start to the end of the flare (Hawley et al. 2014). The coefficient specific to a star is the flare energy with the equivalent duration = 1 (s). Those for AU Mic, YZ CMi, and EV Lac are calculated to be 3.68×10^{32}, 3.56×10^{31}, and 5.25×10^{31} (erg), respectively. We note that
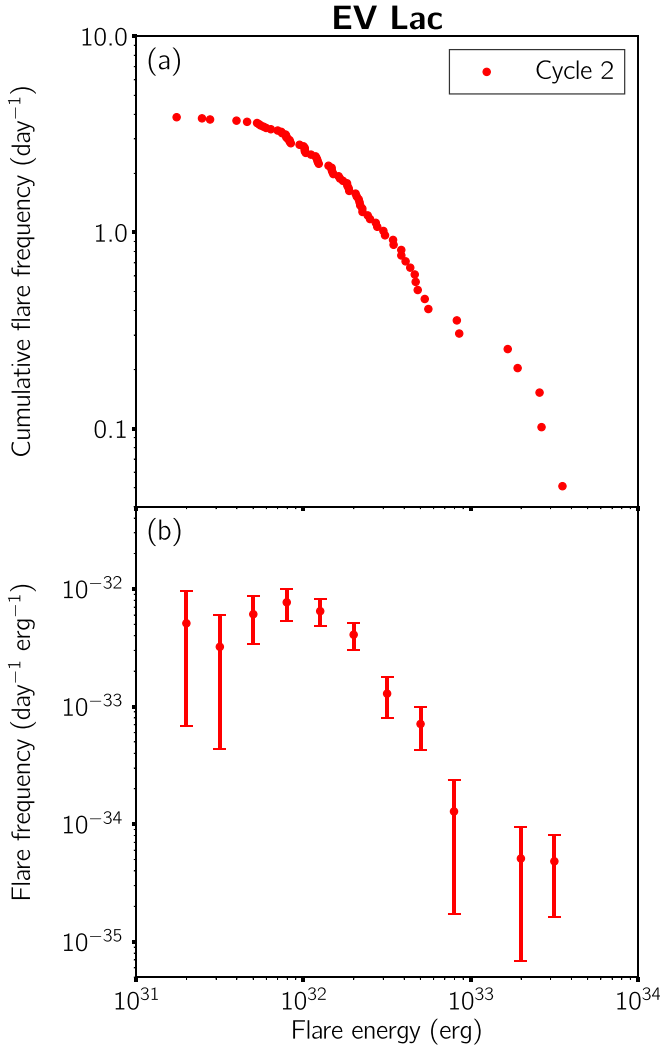
Figure 4. Same as Figure 2 but for EV Lac Cycle 2. The number of flares per observation period of a TESS sector (Sector 16) is $76/19.650 = 3.868$ (day^{-1}).

the calculation error up to a factor is inherent in the assumed flare model (Maehara et al. 2021). Assuming a flare temperature $T_{flare} = 7000$ (K), the energy reduces by a factor of 2. Figures 2, 3, and 4 show the cumulative flare frequency for AU Mic, YZ CMi, and EV Lac, respectively (see Maehara et al. 2021). We discuss the relation between spot locations and flare frequency in Sections 3.2 and 3.3.

2.2. Numerical Setup

Table 1 lists the stellar parameters, references, deduced spot temperature and intensity, and limb-darkening coefficients for AU Mic, YZ CMi, and EV Lac. The spot temperature T_{spot} is deduced from a quadratic formula of the stellar effective temperature T_{eff} (Equation (4) in Herbst et al. 2021):

$$T_{spot} = -3.58 \times 10^{-5} T_{eff}^2 + 0.801 T_{eff} + 666.5. \quad (2)$$

Therefore, the spot relative intensity f_{spot} for the TESS band is calculated by the stellar effective temperature T_{eff} and the spot

temperature T_{spot}:

$$f_{spot} = \frac{\int R(\lambda) B(\lambda, T_{spot}) d\lambda}{\int R(\lambda) B(\lambda, T_{eff}) d\lambda}, \quad (3)$$

where $R(\lambda)$ and $B(\lambda, T)$ are the TESS-band response function and the Planck function with each wavelength λ, respectively. The stellar limb-darkening law is adopted as the following formula for the cosine of the angle to the line of sight μ:

$$I(\mu)/I(1) = 1 - \Sigma_{k=1}^4 c_k (1 - \mu^{k/2}), \quad (4)$$

where the coefficients c_k based on the stellar parameters are deduced from Claret (2018). Then, we adopt the nonlinear limb-darkening law. For the case of EV Lac Cycle 2 as an example, we present the result by the quadratic limb-darkening law (Appendix A.1).

In Paper I, we implemented a code for starspot modeling using an adaptive PT algorithm. The model evidence for each model was also computed with an importance sampling algorithm together with the PT transition. We adopted an analytical spotted model (macula; Kipping 2012) for the spot model, and the model was specified in the stellar and spot parameters: the stellar inclination angle i (deg), the equatorial rotation period P_{eq} (day), the degree of differential rotation κ, the spot relative intensity f_{spot}, the latitude Φ (deg), the initial longitude Λ (deg), the reference time t_{ref} (day; the time at the midpoint of the interval over which the spot has its maximum radius), the maximum radius α_{max} (deg), the emergence duration $\mathcal{I}$ (day), the decay duration $\mathcal{E}$ (day), and the stable duration $\mathcal{L}$ (day). The rotation period at the latitude Φ (Equation (16) in Paper I) was described by

$$P(\Phi) = \frac{P_{eq}}{1 - \kappa \sin^2 \Phi}. \quad (5)$$

In this study, it is unnecessary to adopt the spot parameters of reference time t_p, emergence duration $\mathcal{I}$, decay duration $\mathcal{E}$, and stable duration $\mathcal{L}$ in the model because the amplitudes of the light curves are approximately constant in the observation period of a TESS sector. Therefore, the light curves are specified with fewer stellar and spot parameters than used in Paper I for simplicity (Tables 2, 3, 4, 5, and 6). In fact, we ascertain that the posterior distribution does not converge to a unimodal distribution due to these spot parameters by exploiting test runs. Each spot is discerned by the range of latitude Φ from the southern to the northern pole, not by the range of reference time t_p, as was used in Paper I.

The light curves of AU Mic Cycles 1 and 3, YZ CMi Cycle 3, and EV Lac exhibit two local minima per equatorial rotation period, and we optimize them by two- and three-spot models (Tables 2, 3, 5, and 6). The light curve of YZ CMi Cycle 1 exhibits one local minimum per equatorial rotation period, and we optimize it by two- and one-spot models (Table 4). For the one-spot model, the differential rotation parameter κ is fixed to 0. We note that the light curves of YZ CMi have one local minimum per equatorial rotation period possibly due to its low inclination angle (e.g., Basri & Shah 2020). We have ascertained the posterior distributions of the inclination angle and spot intensity would converge to unphysical modes (the edges of the parameter range) by exploiting test runs because they have respective degeneracies with the spot latitude and radius (Paper I). Therefore, the values of the inclination angle

Table 1
Stellar Parameters

Stellar Parameter	AU Mic	YZ CMi	EV Lac
Effective temperature $T_{\rm eff}$ (K)	3700 ± 100[c]	3100 ± 50[e]	3400 ± 18[g]
Rotation period $P_{\rm rot}$ (day)	4.863 ± 0.010[c]	2.776 ± 0.010[e]	4.359[h]
Stellar radius $R_{\rm star}$ ($R_{\rm Sun}$)	0.75 ± 0.03[c]	$0.37^{+0.03}_{-0.06}$[e]	0.35 ± 0.02[h]
Stellar mass $M_{\rm star}$ ($M_{\rm Sun}$)	0.50 ± 0.03[c]	0.37 ± 0.01[f]	0.35 ± 0.02[h]
Surface gravity $\log g$[a]	4.39 ± 0.10	4.87 ± 0.33	4.89 ± 0.13
Inclination angle i (deg)	75[d]	36^{+17}_{-14}[e]	60[i]
Spot temperature $T_{\rm spot}$ (K)[a]	3140 ± 54	2806 ± 29	2976 ± 10
Spot relative intensity $f_{\rm spot}$[a]	0.43 ± 0.04	0.56 ± 0.03	0.48 ± 0.01
Limb-darkening coefficients (c_1, c_2, c_3, c_4)[b]	$(2.87, -4.35, 3.92, -1.32)$	$(3.15, -4.62, 4.01, -1.34)$	$(3.00, -4.54, 4.01, -1.35)$

Notes.
[a] The surface gravity is calculated from the stellar radius $R_{\rm star}$ and mass $M_{\rm star}$. The spot temperature is formulated by the stellar effective temperature $T_{\rm eff}$ in Equation (2), and the spot relative intensity $f_{\rm spot}$ for the TESS band is deduced from Equation (3).
[b] The stellar limb-darkening coefficient for TESS data is characterized by the effective temperature $T_{\rm eff}$ and surface gravity $\log g$ under solar metallicity (Claret 2018). We adopt coefficient values of ($T_{\rm eff}, \log g$) = (3700, 4.5), (3100, 5.0), and (3400, 5.0) for AU Mic, YZ CMi, and EV Lac, respectively.
[c] Plavchan et al. (2020).
[d] Wisniewski et al. (2019).
[e] Baroch et al. (2020).
[f] Cifuentes et al. (2020).
[g] Rojas-Ayala et al. (2012).
[h] Paudel et al. (2021).
[i] Morin et al. (2008).

Table 2
AU Mic Cycle 1 Case

Deduced Parameters	Two-spot Model	Three-spot Model	Prior Distribution[a]
(Stellar parameters)			
1. Equatorial period $P_{\rm eq}$ (day)	$4.8624^{+0.0001}_{-0.0001}$	$4.8089^{+0.0010}_{-0.0006}$	$\mathcal{U}_{\log}(4.5000, 5.0000)$
2. Degree of differential rotation κ	$-0.0001^{+0.0001}_{-0.0001}$	$0.1998^{+0.0002}_{-0.0022}$	$\mathcal{U}(-0.2000, 0.2000)$
(Spot parameters)			
(First spot)			
3. Latitude Φ_1 (deg)	$-13.54^{+0.12}_{-0.11}$	$-14.72^{+0.11}_{-0.07}$	$\mathcal{U}(-90.00, \Phi_2)$[b]
4. Initial longitude Λ_1 (deg)	$-22.95^{+0.02}_{-0.03}$	$-134.06^{+0.05}_{-0.06}$	$\mathcal{U}(-180.00, 180.00)$
5. Maximum radius $\alpha_{\rm max,1}$ (deg)	$15.61^{+0.01}_{-0.02}$	$12.86^{+0.02}_{-0.01}$	$\mathcal{U}(0.01, 30.00)$
(Second spot)			
6. Latitude Φ_2 (deg)	$39.67^{+0.08}_{-0.07}$	$12.08^{+0.13}_{-0.09}$	$\mathcal{U}(\Phi_1, \Phi_3)$[b]
7. Initial longitude Λ_2 (deg)	$-152.49^{+0.02}_{-0.02}$	$179.39^{+0.06}_{-0.12}$	$\mathcal{U}(-180.00, 180.00)$
8. Maximum radius $\alpha_{\rm max,2}$ (deg)	$16.02^{+0.01}_{-0.01}$	$10.90^{+0.01}_{-0.02}$	$\mathcal{U}(0.01, 30.00)$
(Third spot)			
9. Latitude Φ_3 (deg)	⋯	$13.92^{+0.10}_{-0.10}$	$\mathcal{U}(\Phi_2, 90.00)$[b]
10. Initial longitude Λ_3 (deg)	⋯	$-24.31^{+0.03}_{-0.02}$	$\mathcal{U}(-180.00, 180.00)$
11. Maximum radius $\alpha_{\rm max,3}$ (deg)	⋯	$14.47^{+0.01}_{-0.01}$	$\mathcal{U}(0.01, 30.00)$
Average flux $F_{\rm ave}$	0.831	0.830	
Logarithm of model evidence $\log \mathcal{Z}$	$-63,950.957$	**$-41,382.031$[c]**	

Notes.
[a] $\mathcal{U}_{\log}(a, b) = 1/(\theta \log(b/a))$ and $\mathcal{U}(a, b) = 1/(b-a)$ represent the bounded log uniform distribution (Jeffreys prior) and bounded uniform distribution defined in $a \leqslant \theta \leqslant b$, respectively.
[b] We discern each spot by its latitude Φ_k, not by its reference time t_k as in Paper I, to improve the sampling efficiency of the PT. In the case of the two-spot model, we set $\Phi_3 = 90.0$ (the upper limit of the latitude).
[c] The value of the logarithms of model evidence of the preferable models is marked in boldface.

and spot intensity are fixed to the values in Table 1, and we abbreviate the name used by Paper I for each of the models—for instance, "two-spot model fixed $\sin i$ and $f_{\rm spot}$" in the context of Paper I is simply renamed "two-spot model" in this study. For the case of EV Lac Cycle 2 as an example, we exhibit the result that the spot intensity is included in the parameters under uniform and normal prior distributions (Appendix A.2).

Table 3
AU Mic Cycle 3 Case

Deduced Parameters	Two-spot Model	Three-spot Model	Prior Distribution[a]
(Stellar parameters)			
1. Equatorial period P_{eq} (day)	$4.8289^{+0.0001}_{-0.0002}$	$5.2004^{+0.0112}_{-0.0061}$	$\mathcal{U}_{log}(4.5000, 5.0000)$
2. Degree of differential rotation κ	$0.0094^{+0.0001}_{-0.0001}$	$-0.1072^{+0.0018}_{-0.0032}$	$\mathcal{U}(-0.2000, 0.2000)$
(Spot parameters)			
(First spot)			
3. Latitude Φ_1 (deg)	$-0.55^{+0.18}_{-0.15}$	$-59.04^{+0.06}_{-0.06}$	$\mathcal{U}(-90.00, \Phi_2)$[b]
4. Initial longitude Λ_1 (deg)	$-14.36^{+0.03}_{-0.02}$	$-1.32^{+0.06}_{-0.07}$	$\mathcal{U}(-180.00, 180.00)$
5. Maximum radius $\alpha_{max,1}$ (deg)	$12.80^{+0.01}_{-0.01}$	$30.00^{+0.00}_{-0.01}$	$\mathcal{U}(0.01, 30.00)$
(Second spot)			
6. Latitude Φ_2 (deg)	$80.22^{+0.01}_{-0.01}$	$52.57^{+0.12}_{-0.10}$	$\mathcal{U}(\Phi_1, \Phi_3)$[b]
7. Initial longitude Λ_2 (deg)	$-153.29^{+0.04}_{-0.03}$	$164.28^{+0.13}_{-0.14}$	$\mathcal{U}(-180.00, 180.00)$
8. Maximum radius $\alpha_{max,2}$ (deg)	$30.00^{+0.00}_{-0.01}$	$16.42^{+0.02}_{-0.04}$	$\mathcal{U}(0.01, 30.00)$
(Third spot)			
9. Latitude Φ_3 (deg)	...	$56.28^{+0.05}_{-0.05}$	$\mathcal{U}(\Phi_2, 90.00)$[b]
10. Initial longitude Λ_3 (deg)	...	$-96.59^{+0.09}_{-0.11}$	$\mathcal{U}(-180.00, 180.00)$
11. Maximum radius $\alpha_{max,3}$ (deg)	...	$16.13^{+0.03}_{-0.03}$	$\mathcal{U}(0.01, 30.00)$
Average flux F_{ave}	0.816	0.823	
Logarithm of model evidence $\log \mathcal{Z}$	$-139,256.404$	$\mathbf{-85,746.962}$[c]	

Notes.

[a] $\mathcal{U}_{log}(a, b) = 1/(\theta \log(b/a))$ and $\mathcal{U}(a, b) = 1/(b - a)$ represent the bounded log uniform distribution (Jeffreys prior) and bounded uniform distribution defined in $a \leqslant \theta \leqslant b$, respectively.

[b] We discern each spot by its latitude Φ_k, not by its reference time t_k as in Paper I, to improve the sampling efficiency of the PT. In the case of the two-spot model, we set $\Phi_3 = 90.0$ (the upper limit of the latitude).

[c] The value of the logarithms of model evidence of the preferable models is marked in boldface.

3. Results and Discussion

We optimize the light curves of AU Mic Cycles 1 and 3, YZ CMi Cycle 3, and EV Lac Cycle 2 by two- and three-spot models and the light curve of YZ CMi Cycle 1 by two- and one-spot models. The number of spots is set as the number of local minima in the light curve and the number plus one (Section 2.2). For every case, unimodal posterior distributions are deduced regardless of the number of spots, and joint ones are delineated in Appendix B. Tables 2, 3, 4, 5, and 6 show the modes of the deduced posterior distributions, their credible regions, the reproduced average flux, and the logarithm of model evidence for each model, together with the prior distribution for each of the parameters, for AU Mic Cycles 1 and 3, YZ CMi Cycles 1 and 3, and EV Lac Cycle 2, respectively. The values of the logarithms of model evidence of the preferable models are marked in boldface. Figure 1 exhibits the reproduced light curves with each mode of the posterior distributions in each of the two-spot model for each (red). All light curves can be folded in phase with the rotation period since the deduced degree of differential rotation κ is approximately 0 or the absolute value of spot latitudes is almost the same value, and the amplitude of the light curve is approximately constant in the observation period of a TESS sector. Figures 5, 6, 7, 8, and 9 exhibit the visualized surface reproduced with each mode of the posterior distributions: (a), (f) the phase-folded light curve (black) and the reproduced one with the model (red); (b), (g) the temporal variation of the visible projected area of each spot (red, blue, and green) and the total area (black) relative to the stellar disk or solar hemisphere; (c), (h) the temporal variation of the visible area

but relative to the stellar or solar hemispheres ; (d) the flare frequency in each bin for all flares (red) and for flares with larger equivalent duration than 1 (s) (blue); and (e) the flare energy in each bin for those flares. We discuss the result in comparison with those of other studies by photometry and spectroscopy in Section 3.1, the correlation between spot locations and flare frequency in Section 3.2, the two-year variation of the light curves for AU Mic and YZ CMi in Section 3.3, and the model selection and the validity of starspot modeling in Section 3.4.

3.1. Deduced Parameters in Comparison with Other Studies by Photometry and Spectroscopy

AU Mic. In the two-spot models (Tables 2 and 3), the separation of spot longitude extends from 129.54 ± 0.04 (deg) for Cycle 1 to 138.93 ± 0.05 (deg) for Cycle 3. This slight change in the separation can be attributed to the differential rotation assuming that the same spots have existed for two years and the star has significant differential rotation. In contrast, the deduced degree of differential rotation κ for Cycles 1 and 3 is approximately 0. This value of the differential rotation cannot cause the change in the separation of the spots. This may mean that the change in the relative longitude of the two spots can be caused by factors other than the differential rotation, although we need to pay attention to this small value because the observation period of a TESS sector (~ 27 days) is not enough for us to deduce the differential rotation accurately.

Wisniewski et al. (2019) also conducted starspot modeling for the same light curve with two spots using the STSP code (Davenport et al. 2015). Their results of deduced spot latitudes

Table 4
YZ CMi Cycle 1 Case

Deduced Parameters	Two-spot Model	One-spot Model	Prior Distribution[a]
(Stellar parameters)			
1. Equatorial period $P_{\rm eq}$ (day)	$2.7753^{+0.0002}_{-0.0003}$	$2.7737^{+0.0001}_{-0.0001}$	$\mathcal{U}_{\log}(2.0000, 3.0000)$
2. Degree of differential rotation κ	$-0.0008^{+0.0002}_{-0.0002}$	0.0000 (*fixed*)	$\mathcal{U}(-0.2000, 0.2000)$
(Spot parameters)			
(First spot)			
3. Latitude Φ_1 (deg)	$-6.60^{+0.24}_{-0.19}$	$79.03^{+0.01}_{-0.02}$	$\mathcal{U}(-90.00, \Phi_2)$[b]
4. Initial longitude Λ_1 (deg)	$113.68^{+0.20}_{-0.22}$	$31.35^{+0.06}_{-0.06}$	$\mathcal{U}(-180.00, 180.00)$
5. Maximum radius $\alpha_{\rm max,1}$ (deg)	$12.73^{+0.07}_{-0.08}$	$29.99^{+0.01}_{-0.02}$	$\mathcal{U}(0.01, 30.00)$
(Second spot)			
6. Latitude Φ_2 (deg)	$41.17^{+0.30}_{-0.28}$	...	$\mathcal{U}(\Phi_1, 90.00)$[b]
7. Initial longitude Λ_2 (deg)	$17.36^{+0.12}_{-0.18}$	...	$\mathcal{U}(-180.00, 180.00)$
8. Maximum radius $\alpha_{\rm max,2}$ (deg)	$15.92^{+0.01}_{-0.02}$	...	$\mathcal{U}(0.01, 30.00)$
Average flux $F_{\rm ave}$	0.839	0.778	
Logarithm of model evidence $\log\mathcal{Z}$	**14,982.598**[c]	4625.639	

Notes.

[a] $\mathcal{U}_{\log}(a, b) = 1/(\theta\log(b/a))$ and $\mathcal{U}(a, b) = 1/(b - a)$ represent the bounded log uniform distribution (Jeffreys prior) and bounded uniform distribution defined in $a \leqslant \theta \leqslant b$, respectively.

[b] We discern each spot by its latitude Φ_k, not by its reference time t_k as in Paper I, to improve the sampling efficiency of the PT. In the case of the one-spot model, we set $\Phi_2 = 90.0$ (the upper limit of the latitude).

[c] The value of the logarithms of model evidence of the preferable models is marked in boldface.

$\simeq$9.6 and 44.8 (deg) are different from our results $=-13.5^{+0.1}_{-0.2}$ and $39.7^{+0.1}_{-0.1}$ (deg) probably due to the following three factors: (i) the high inclination angle $i = 75$ (deg) can result in large uncertainty in deducing spot latitudes; (ii) we set the spot relative intensity $f_{\rm spot} = 0.43$ (Table 1) by calculating the intensity in the TESS band based on the spot temperature deduced from the formula (Equations (2) and (3)), whereas Wisniewski et al. (2019) assumed 0.7 (Davenport et al. 2015), which resulted in a difference due to degeneracies between the spot relative intensity and latitude (Paper I); and (iii) it is also difficult to discern whether a spot is in the northern or the southern hemisphere as the inclination angle increases (Walkowicz et al. 2013). In addition, the difference in the deduced spot longitude in our result $=129.54 \pm 0.04$ (deg) is consistent with their result that the spots are separated by 131 (deg). This consistency in the longitude is simply understood since the local minima of the light curve only correspond to the separation of spot longitude in the case of the two-spot model.

The surface map has been investigated through Doppler imaging and Zeeman Doppler imaging between Cycles 1 and 3 (2019 September to November; Klein et al. 2021) and after Cycle 3 (2020 November to 2021 September; Klein et al. 2022). On the basis of the Doppler imaging, Klein et al. (2021) reported there were two dark features from the equator and 40 (deg) in addition to a bright one around the equator opposite to a dark one in 2019. Klein et al. (2022) reported there were also dark features at the equator and 60 (deg) in 2020. These results

are different from our results of deduced latitudes for Cycles 1 and 3 in the two-spot model. It should be noted that the result of Wisniewski et al. (2019) is almost consistent with the results of the Doppler imaging. One reason for this difference between our result and their result by Doppler imaging could be that there are degeneracies between the inclination angle and latitude, especially given the high inclination angle $i = 75$ (deg) (Walkowicz et al. 2013), in the starspot modeling. We need to be careful in interpreting these results obtained by both starspot modeling and Doppler imaging because these results largely depend on the mapping method and assumptions, such as on the prior distribution (Roettenbacher et al. 2017; Luger et al. 2021).

In the three-spot models (Tables 2 and 3), the latitudes in each model are almost the same absolute values. The rotation period of each spot has almost the same value because the spot has almost the same latitude (Equation (5)), and therefore the degree of differential rotation cannot be measured accurately, although large absolute values are deduced for Cycles 1 and 3.

YZ CMi. In the two-spot models (Tables 4 and 5), the separation of spot longitude extends from 96.32 ± 0.28 (deg) for Cycle 1 to 193.95 ± 0.53 (deg) for Cycle 3. As in AU Mic, this slight change in the separation can be attributed to the differential rotation assuming that the same spots have existed for two years and the star has significant differential rotation. In contrast, the deduced degree of differential rotation κ is approximately 0. This may mean that the change in the relative

Table 5
YZ CMi Cycle 3 Case

Deduced Parameters	Two-spot Model	Three-spot Model	Prior Distribution[a]
(Stellar parameters)			
1. Equatorial period P_{eq} (day)	$2.7705^{+0.0003}_{-0.0002}$	$2.7707^{+0.0003}_{-0.0003}$	$\mathcal{U}_{log}(2.0000, 3.0000)$
2. Degree of differential rotation κ	$0.0082^{+0.0007}_{-0.0008}$	$0.0088^{+0.0016}_{-0.0011}$	
$\mathcal{U}(-0.2000, 0.2000)$	(Spot parameters)		
(First spot)			
3. Latitude Φ_1 (deg)	$18.48^{+0.28}_{-0.30}$	$-10.92^{+0.50}_{-0.45}$	$\mathcal{U}(-90.00, \Phi_2)$[b]
4. Initial longitude Λ_1 (deg)	$-23.68^{+0.17}_{-0.15}$	$133.41^{+0.81}_{-0.66}$	
$\mathcal{U}(-180.00, 180.00)$	5. Maximum radius $\alpha_{max,1}$ (deg)	$12.91^{+0.06}_{-0.05}$	$7.91^{+0.14}_{-0.19}$
$\mathcal{U}(0.01, 30.00)$			
(Second spot)			
6. Latitude Φ_2 (deg)	$38.82^{+1.21}_{-0.81}$	$16.36^{+0.36}_{-0.29}$	$\mathcal{U}(\Phi_1, \Phi_3)$[b]
7. Initial longitude Λ_2 (deg)	$170.27^{+0.50}_{-0.50}$	$-17.50^{+0.35}_{-0.52}$	
$\mathcal{U}(-180.00, 180.00)$	8. Maximum radius $\alpha_{max,2}$ (deg)	$7.77^{+0.12}_{-0.10}$	$12.34^{+0.05}_{-0.05}$
$\mathcal{U}(0.01, 30.00)$			
(Third spot)			
9. Latitude Φ_3 (deg)	⋯	$49.48^{+5.76}_{-2.69}$	$\mathcal{U}(\Phi_2, 90.00)$[b]
10. Initial longitude Λ_3 (deg)	⋯	$-146.64^{+2.46}_{-2.57}$	
$\mathcal{U}(-180.00, 180.00)$	11. Maximum radius $\alpha_{max,3}$ (deg)	⋯	$6.59^{+0.41}_{-0.18}$
$\mathcal{U}(0.01, 30.00)$			
Average flux F_{ave}	0.847	0.848	
Logarithm of model evidence $\log\mathcal{Z}$	13,111.858	**13,492.544**[c]	

Notes.

[a] $\mathcal{U}_{log}(a, b) = 1/(\theta\log(b/a))$ and $\mathcal{U}(a, b) = 1/(b - a)$ represent the bounded log uniform distribution (Jeffreys prior) and bounded uniform distribution defined in $a \leqslant \theta \leqslant b$, respectively.

[b] We discern each spot by its latitude Φ_k, not by its reference time t_k as in Paper I, to improve the sampling efficiency of the PT. In the case of the two-spot model, we set $\Phi_3 = 90.0$ (the upper limit of the latitude).

[c] The value of the logarithms of model evidence of the preferable models is marked in boldface.

longitude of the two spots can be caused by factors other than the differential rotation, although we need to pay attention to this small value because the observation period of a TESS sector (∼27 days) is not enough for us to deduce the differential rotation accurately, as discussed for AU Mic.

Bicz et al. (2022) also conducted starspot modeling for the same light curves with three and four spots for Cycles 1 and 3 using the BASSMAN code, respectively. Their model is different in that they assumed an inclination angle = 60 (deg) and deduced the spot temperature (i.e., the relative intensity) for each spot, whereas we set the angle $i = 36$ (deg) and the spot temperature $T_{spot} = 2806$ (K) (relative intensity $f_{spot} = 0.66$) for all spots. We do not respectively adopt three- and four-spot models for Cycles 1 and 3, and our result of the deduced spot parameter is very different from their result. The difference is due to the models and assumptions, such as on the number of spots (see Section 3.4).

The surface map has been investigated through Doppler imaging before Cycle 1 (2016 September to 2017 May; Baroch et al. 2020). The result suggests there are spots on the latitude from 75 to 81 (deg), and this result is consistent with our result

of deduced latitudes $=79.0^{+0.01}_{-0.02}$ (deg) for Cycle 1 in the one-spot model.

EV Lac. The surface map has been investigated through Doppler imaging before Cycle 2 (2016 January to 2017 December; Jeffers et al. 2022). The result suggests that there are spots near the north pole, and is different from our result of deduced latitudes in both the two- and three-spot models (Table 6).

3.2. Spot Location versus Flare Frequency

We investigate the correlation between spot locations and flare frequency in each rotation phase of the light curve. In Figures 5, 6, 7, 8, and 9, for each flare in the phase-folded light curve, we assume a null hypothesis that the flare is evenly distributed across 10 bins of the rotation phase and perform a chi-squared test with 9 degrees of freedom. For AU Mic Cycles 1 and 3, YZ CMi Cycles 1 and 3, and EV Lac Cycle 2, we obtain a reduced chi-square = 0.899 (0.824), 0.381 (0.533), 0.505 (0.376), 0.439 (0.444), and 0.825 (0.890) and a *p*-value = 0.525 (0.594), 0.945 (0.851), 0.872 (0.947), 0.915 (0.911), and 0.593 (0.533) for all flares (for flares with longer

Table 6
EV Lac Cycle 2 Case

Deduced Parameters	Two-spot Model	Three-spot Model	Prior Distribution[a]
(Stellar parameters)			
1. Equatorial period P_{eq} (day)	$4.3573^{+0.0002}_{-0.0003}$	$4.3651^{+0.0003}_{-0.0002}$	$\mathcal{U}_{log}(4.0000, 5.0000)$
2. Degree of differential rotation κ	$0.0020^{+0.0001}_{-0.0001}$	$-0.0033^{+0.0001}_{-0.0001}$	
$\mathcal{U}(-0.2000, 0.2000)$	(Spot parameters)		
(First spot)			
3. Latitude Φ_1 (deg)	$24.89^{+0.28}_{-0.21}$	$9.91^{+0.12}_{-0.18}$	$\mathcal{U}(-90.00, \Phi_2)$[b]
4. Initial longitude Λ_1 (deg)	$60.35^{+0.11}_{-0.13}$	$-113.64^{+0.20}_{-0.20}$	
$\mathcal{U}(-180.00, 180.00)$	5. Maximum radius $\alpha_{max,1}$ (deg)	$13.44^{+0.02}_{-0.02}$	$14.67^{+0.04}_{-0.06}$
$\mathcal{U}(0.01, 30.00)$			
(Second spot)			
6. Latitude Φ_2 (deg)	$55.89^{+0.31}_{-0.26}$	$9.95^{+0.16}_{-0.13}$	$\mathcal{U}(\Phi_1, \Phi_3)$[b]
7. Initial longitude Λ_2 (deg)	$-84.11^{+0.11}_{-0.11}$	$111.85^{+0.32}_{-0.35}$	
$\mathcal{U}(-180.00, 180.00)$	8. Maximum radius $\alpha_{max,2}$ (deg)	$14.36^{+0.06}_{-0.06}$	$10.56^{+0.07}_{-0.09}$
$\mathcal{U}(0.01, 30.00)$			
(Third spot)			
9. Latitude Φ_3 (deg)	...	$54.15^{+0.53}_{-0.47}$	$\mathcal{U}(\Phi_2, 90.00)$[b]
10. Initial longitude Λ_3 (deg)	...	$13.71^{+0.36}_{-0.25}$	
$\mathcal{U}(-180.00, 180.00)$	11. Maximum radius $\alpha_{max,3}$ (deg)	...	$15.99^{+0.06}_{-0.04}$
$\mathcal{U}(0.01, 30.00)$			
Average flux F_{ave}	0.850	0.842	
Logarithm of model evidence $\log \mathcal{Z}$	-7297.802	**-4135.585**[c]	

Notes.
[a] $\mathcal{U}_{log}(a, b) = 1/(\theta \log(b/a))$ and $\mathcal{U}(a, b) = 1/(b - a)$ represent the bounded log uniform distribution (Jeffreys prior) and bounded uniform distribution defined in $a \leqslant \theta \leqslant b$, respectively.
[b] We discern each spot by its latitude Φ_k, not by its reference time t_k as in Paper I, to improve the sampling efficiency of the PT. In the case of the two-spot model, we set $\Phi_3 = 90.0$ (the upper limit of the latitude).
[c] The value of the logarithms of model evidence of the preferable models is marked in boldface.

equivalent duration than 1 s), respectively. Thus, the hypothesis that the flares are evenly distributed across 10 bins is not rejected, and we cannot conclude that there is a correlation between the rotation phase of the light curve and the occurrence of flares. This result is consistent with the result in previous studies for different stars (Hawley et al. 2014; Doyle et al. 2018, 2020).

In contrast, Bicz et al. (2022) suggested that the hypothesis that flares are evenly distributed in the rotation phase cannot be rejected for 80 flares in Cycle 1 and can be rejected for 80 flares in Cycle 3. Our result is different from their result because more flares are detected in our study: 124 in Cycle 1 and 137 in Cycle 3 (Section 2.1).

As a result of the starspot modeling, we can interpret the correlation between rotation phases and flare frequency as follows. Our result shows that either spot is always visible in all phases (Figures 5, 6, 7, 8, and 9) due to multiple spots or a moderate inclination angle for each star. This suggests that flare frequency can be less correlated with the rotation phase

assuming that flares occur around spots visible to the line of sight at that time. Therefore, a polar spot is not necessarily needed to explain that flares are distributed in all rotation phases, and no or low correlation between rotation phases and flare frequency does not mean no relation between spot locations and flare occurrence.

3.3. Two-year Variation of Light Curves

AU Mic and YZ CMi were observed in TESS Cycles 1 and 3 with an interval of approximately two years. It is shown that the amplitude of both light curves decreases (Figure 1), and the flare frequency is almost constant within an error (Figures 2 and 3).[15] In particular, the light curve of YZ CMi changes from one to two local minima per equatorial rotation period. Therefore, we compare the starspot modeling of Cycle 1 with

---

[15] We note that, when the frequency is compared, the flare frequency should be adopted rather than the cumulative flare frequency because the latter highly depends on large flares.
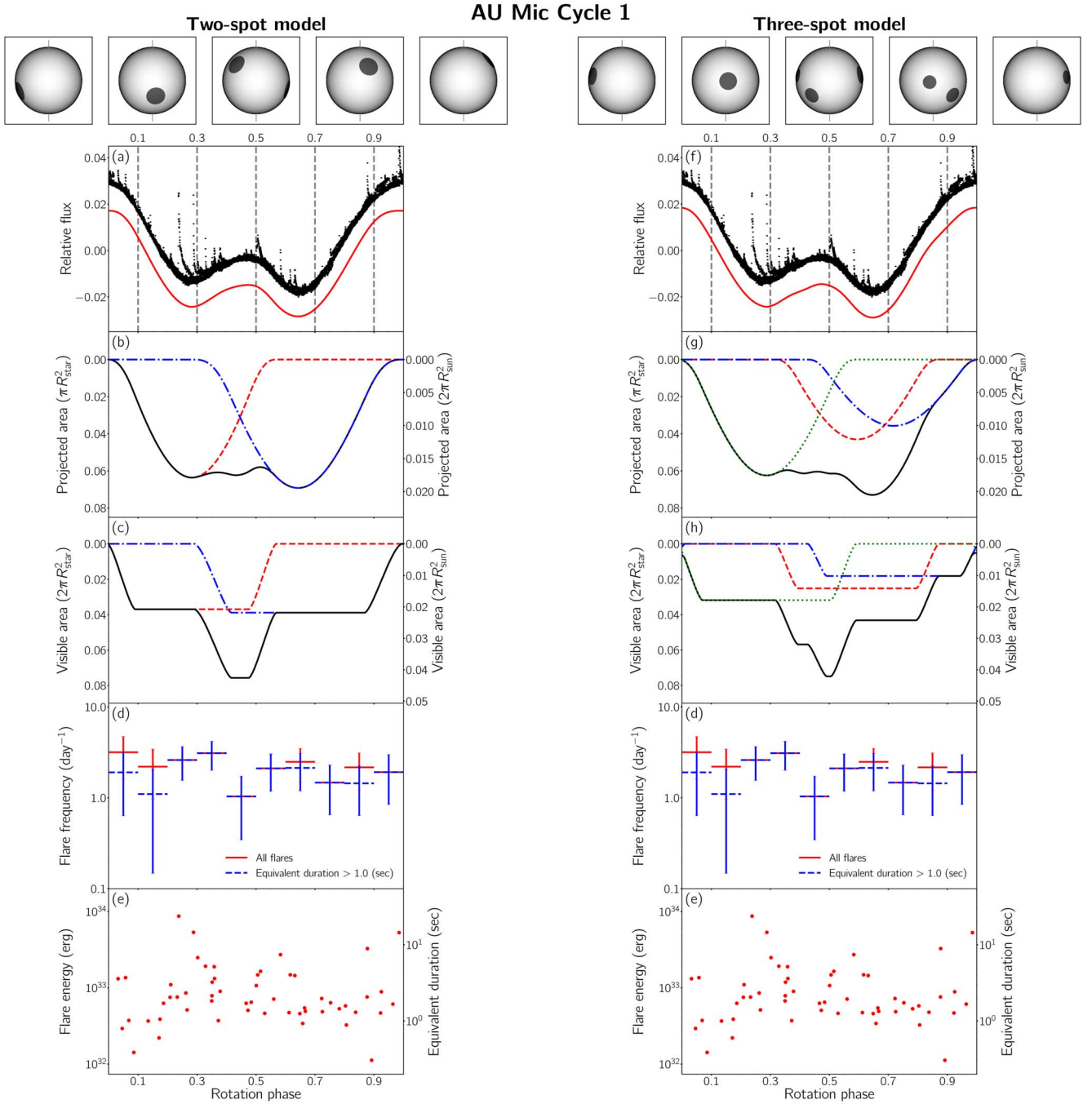
Figure 5. (Left) Visualized surface reproduced with each mode of the posterior distributions for rotation phases = 0.1, 0.3, 0.5, 0.7, and 0.9 (vertical dashed lines). The light curve is folded with the period = 4.862 (days) from the day of the first peak = 1329.1 (BJD 2,457,000): (a) the phase-folded light curve of AU Mic Cycle 1 (black) and the phase-folded reproduced one with the two-spot model (red), (b) the temporal variation of the visible projected area of each spot (red, blue, and green) and the total area (black) relative to the stellar disk or solar hemisphere, (c) same as (b) but for the visible area relative to the stellar or solar hemispheres, (d) the flare frequency per day in each bin for all flares (red) and for flares with larger equivalent duration than 1.0 (s) (blue; the error bar equals the square root of (the number of flares in each bin + 1) per observation period), and (e) the flare energy and the corresponding equivalent duration in each bin. (Right) (f)–(h) Same as (a)–(c) but for the three-spot model.

that of Cycle 3 for AU Mic and YZ CMi in terms of spot latitude and size to explain the variations of light curves ascribed to spots in the two years between the different TESS cycles. Then, we focus on the result of the two-spot model because two-spot models are adopted for Cycles 1 and 3.

Comparing the two-spot models for AU Mic (Tables 2 and 3), we find the deduced latitudes and radii are quite different. Although the latitude and radius of the first spot near the

equator respectively correspond within an error of 14 and 3 (deg), the latitude of the second spot changes from midlatitude to the pole. The radius of the second spot on the pole is not determined due to the unspotted level of the light curve. We describe the unspotted level on the starspot modeling below.

Comparing the two-spot models for YZ CMi (Tables 4 and 5), we find the deduced latitudes and radii are slightly different. The latitude of the first spot near the equator is different within
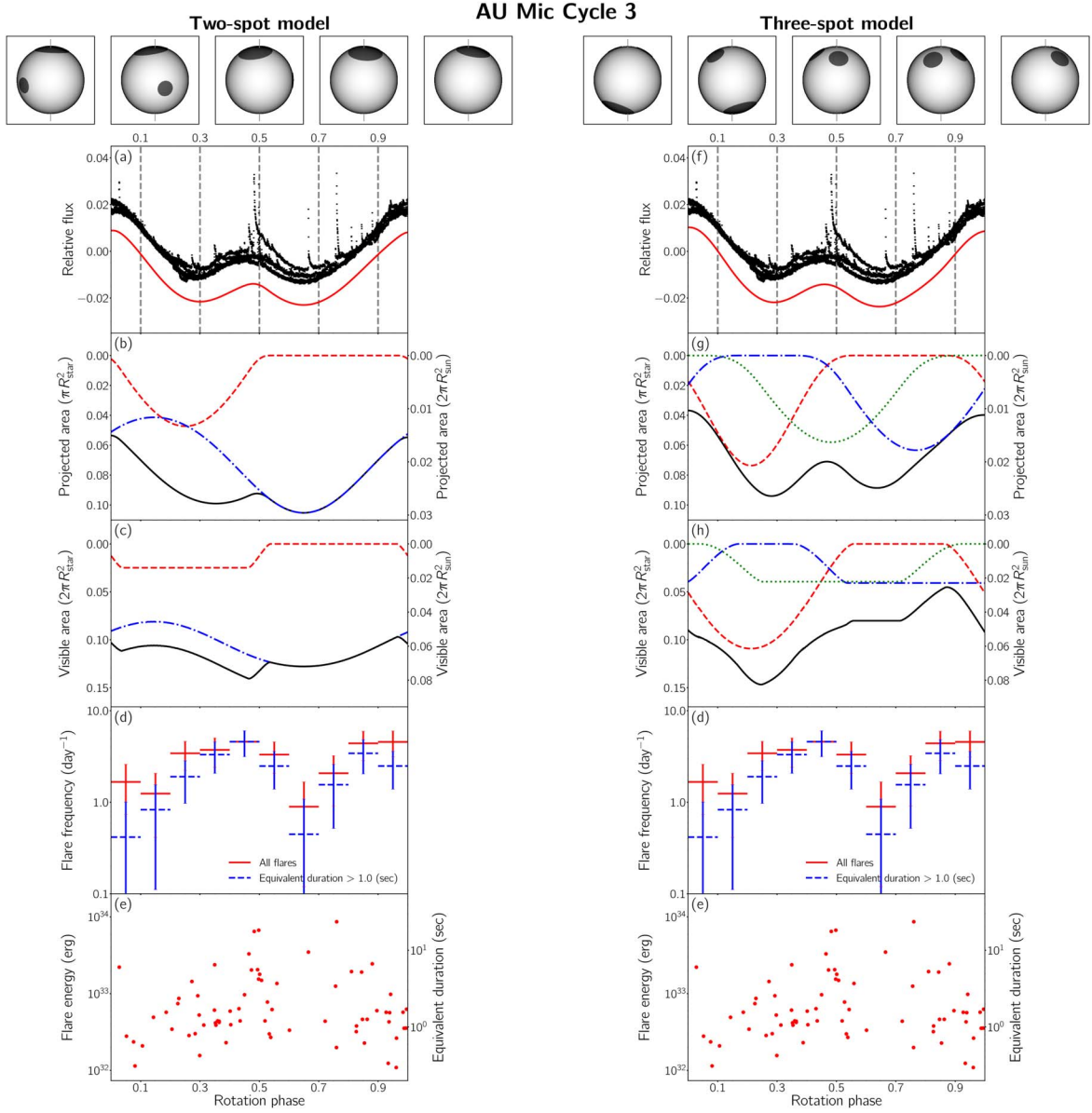
Figure 6. Same as Figure 5 but for AU Mic Cycle 3 with the period = 4.829 (days) from the day of the first peak = 2040.1 (BJD 2,457,000).

an error of 25 (deg), and that of the second one at midlatitude is different within an error of 5 (deg) because the latitude is determined by the visible duration of the spot (Walkowicz et al. 2013). It is possible that the second spot decayed and the relative longitude changed due to the stellar differential rotation or the spot in Cycle 1 decayed and a new spot emerged in the interval between Cycles 1 and 3.

The total visible area relative to the stellar hemisphere $(2\pi R_{star}^2$; Figures 5, 6, 7, and 8) changed from 0.076 to 0.142 for AU Mic and from 0.063 to 0.035 for YZ CMi. We find that the flare frequency did not change from Cycle 1 to Cycle 3 for both AU Mic and YZ CMi (Figures 2 and 3). We suggest that this may be because the spot area deduced from the starspot modeling changed by a factor of 2 in two years, but this could not affect and change the flare frequency within the error.

We note that it is difficult to determine the area of always visible spots on high latitude and the existence of a polar spot because such spots reduce the average flux and do not significantly contribute to the modulation of the light curve.

Thus, the unspotted level is not well determined in our result. The unspotted level of flux is of importance to estimating the spot area and other spot parameters in starspot modeling. For the two-spot (three- or one-spot) models (Tables 2, 3, 4, 5, and 6), the reproduced average fluxes F_{ave} are 0.831 (0.830), 0.816 (0.823), 0.839 (0.778), 0.847 (0.848), and 0.850 (0.842), respectively. Then, the fluxes of Cycle 3 relative to those of Cycle 1 for AU Mic and YZ CMi are 0.982 and 1.010, respectively. This reflects the fact that the spot area has become smaller or an always visible polar spot that does not contribute to the brightness change has appeared, and the amplitude of the light curve has become smaller from Cycle 1 to 3. The reason why the radii of the polar spots reach the upper limit of the parameter range is that the unspotted level is not determined, and the same light curve can be reproduced by reducing the average flux. Therefore, it can be validated that there is only a polar spot in the two- and three-spot models for AU Mic Cycle 3. The possible large spot at high latitude could affect the above
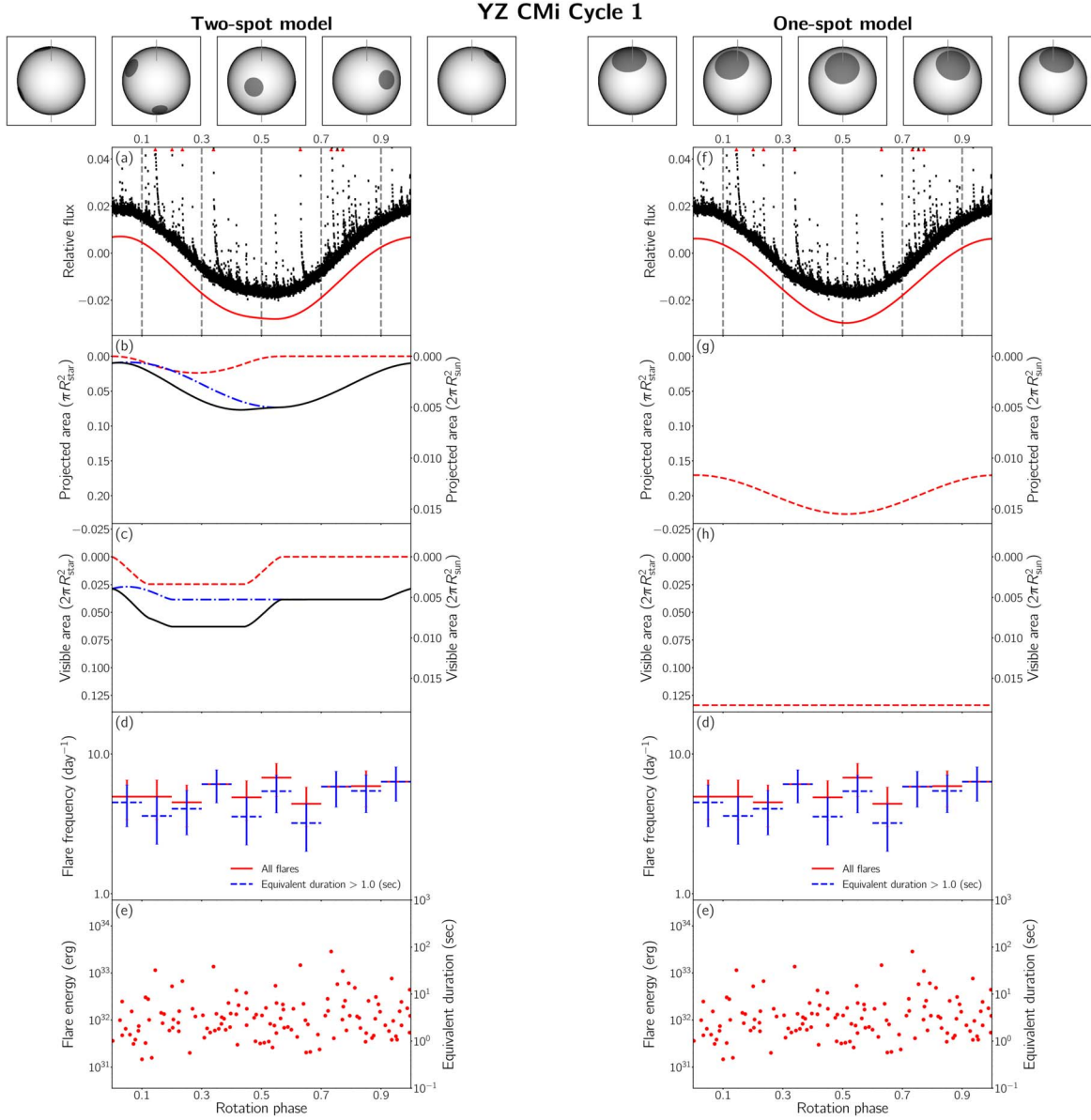
Figure 7. (Left) Visualized surface reproduced with each mode of the posterior distributions for rotation phases = 0.1, 0.3, 0.5, 0.7, and 0.9 (vertical dashed lines). The light curve is folded with the period = 2.774 (days) from the day of the first peak = 1498.3 (BJD 2,457,000): (a) the phase-folded light curve of YZ CMi Cycle 1 (black) with large flares marked as outliers (red triangles) and the phase-folded reproduced one with the two-spot model (red), (b) the temporal variation of the visible projected area of each spot (red, blue, and green) and the total area (black) relative to the stellar disk or solar hemisphere, (c) same as (b) but for the visible area relative to the stellar or solar hemispheres, (d) the flare frequency per day in each bin for all flares (red) and for flares with larger equivalent duration than 1.0 (s) (blue; the error bar equals the square root of (the number of flares in each bin + 1) per observation period), and (e) the flare energy and the corresponding equivalent duration in each bin. (Right) Same as the left but for the one-spot model.

conclusion (i.e., the change of the total spot area in two years), and more in-depth analysis may be necessary.

3.4. Model Selection and the Validity of Starspot Modeling

More spots are indicated to be on the surface than the number of local minima per equatorial rotation period by analyses of spot occultations (Morris et al. 2017; Namekata et al. 2020). In other words, the light curves of spotted stars always have two or one local minimum per equatorial rotation period even if produced with any number of spots, but not two or one spot is actually present on the surface (Basri 2018; Basri & Nguyen 2018; Luger et al. 2021a, 2021b). Then, as in Paper I, we compare the number of spots based on the model

selection by comparing the model evidence (Kass & Raftery 1995). The values of the logarithm of model evidence $\log \mathcal{Z}$ for AU Mic Cycles 1 and 3, YZ CMi Cycles 1 and 3, and EV Lac Cycle 2 are listed in Tables 2, 3, 4, 5, and 6, respectively.

In the cases of AU Mic Cycles 1 and 3, YZ CMi Cycle 3, and EV Lac Cycle 2, the three-spot model is much more decisive than the two-spot model by orders of magnitude: the evidences of the three-spot model relative to those of the two-spot model are $\Delta \log \mathcal{Z} = 22,568.926$, 53,509.442, 380.686, and 3162.217, respectively. In the case of YZ CMi Cycle 1, the two-spot model is much more decisive than the one-spot model by orders of magnitude: the evidence of the two-spot model relative to that of the one-spot model is $\Delta \log \mathcal{Z} =$
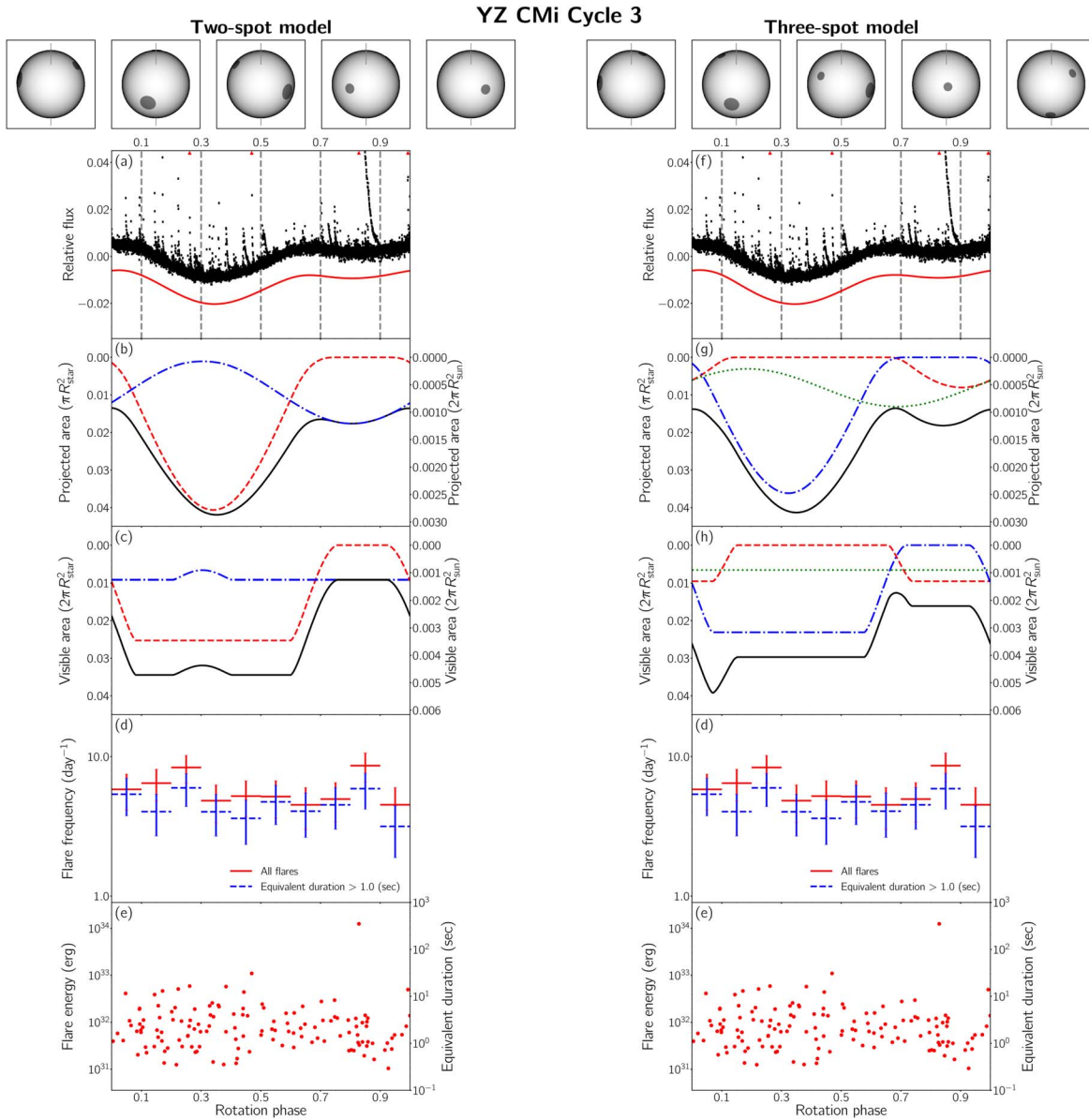
Figure 8. Same as Figure 7 but for YZ CMi Cycle 3 with the period = 2.773 (days) from the day of the first peak = 2231.1 (BJD 2,457,000).

10, 356.959 . In all cases, it is suggested that each of the models with one additional spot is preferable in the Bayesian framework. While we can also conduct starspot modeling with an additional spot, models with less than three spots are sufficient for investigating the correlation between the spot location and flare frequency (Section 3.2). We note that the model evidence is affected by the choice of prior distribution (Gelman et al. 1995). To constrain the number of spots precisely, it is also essential to scan the surface with spot occultations by multiple transits of exoplanets (Morris et al. 2017; Namekata et al. 2020; Bruno & Deleuil 2021).

The peak-to-trough amplitudes of light curves for AU Mic Cycles 1 and 3, YZ CMi Cycles 1 and 3, and EV Lac Cycle 2 are 0.046 (0.049), 0.032 (0.035), 0.035 (0.036), 0.014 (0.015), and 0.027 (0.028) for the two-spot model (three- or one-spot model), respectively. According to Figure 4 in Rackham et al. (2018), the peak-to-trough amplitude can be only explained by giant spots on the surface when the filling factors are approximately 0.22, 0.10, 0.12, 0.02, and 0.08,

respectively. Since large-spot groups are necessary to generate large amplitudes of light curves, it is sufficient to assume a few large spots for M-dwarf stars.

In addition, Roettenbacher et al. (2017) showed that a comparison between light-curve inversion and Doppler imaging for the RS CVn star σ Geminorum reveals a qualitatively different surface map is obtained due to the various degeneracies inherent in each method. Therefore, as future studies, multicolor and multispectrum mappings of the stellar surface are important to constrain the surface map more robustly.

4. Conclusion and Future Prospects

We conducted starspot modeling for the TESS light curves of three M-dwarf flare stars, AU Mic, YZ CMi, and EV Lac, using the code implemented in Paper I, for the purpose of investigating the spot properties and their relation to flare occurrences. The code enables us to deduce multiple stellar/
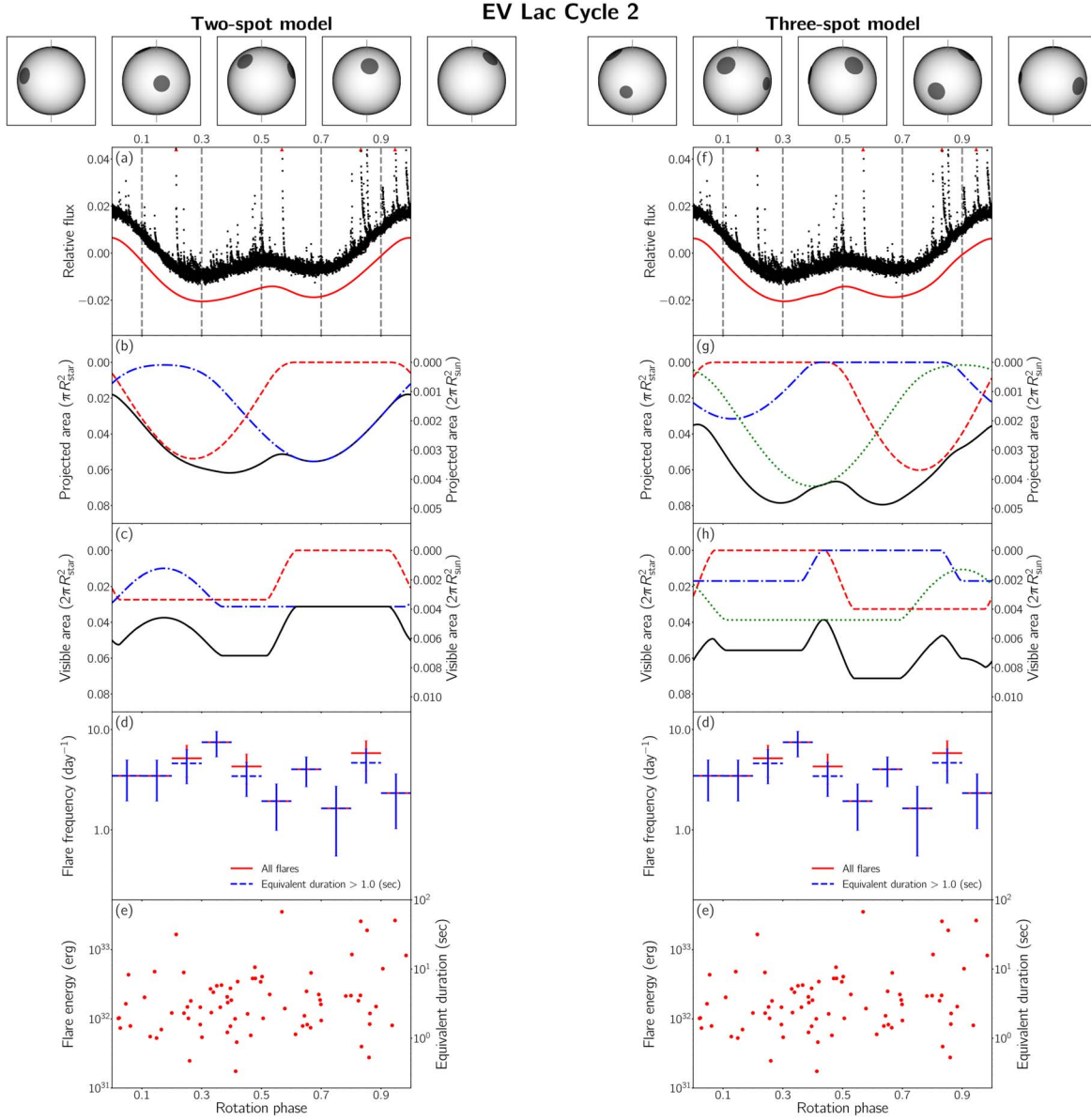
Figure 9. (Left) Visualized surface reproduced with each mode of the posterior distributions for rotation phases = 0.1, 0.3, 0.5, 0.7, and 0.9 (vertical dashed lines). The light curve is folded with the period = 4.359 (days) from the day of the first peak = 1741.1 (BJD 2,457,000): (a) the phase-folded light curve of EV Lac Cycle 2 (black) with large flares marked as outliers (red triangles) and the phase-folded reproduced one with the two-spot model (red), (b) the temporal variation of the visible projected area of each spot (red, blue, and green) and the total area (black) relative to the stellar disk or solar hemisphere, (c) same as (b) but for the visible area relative to the stellar or solar hemispheres, (d) the flare frequency per day in each bin for all flares (red) and for flares with larger equivalent duration than 1.0 (s) (blue; the error bar equals the square root of (the number of flares in each bin + 1) per observation period), and (e) the flare energy and the corresponding equivalent duration in each bin. (Right) Same as the left but for the three-spot model.

spot parameters by the adaptive PT algorithm efficiently. The light curves of AU Mic Cycles 1 and 3, YZ CMi Cycle 3, and EV Lac Cycle 2 are optimized by the two- and three-spot models, and that of YZ CMi Cycle 1 by the two- and one-spot models. For each model, unimodal posterior distributions are deduced (Tables 2, 3, 4, 5, and 6) regardless of the number of spots, and joint ones are delineated in Appendix B. Flares are also detected (Figure 1) and accumulated to obtain the flare frequency (Figures 2, 3, and 4). We discuss the results in terms of comparison with previous studies by photometry and spectroscopy, the relation between spot locations and flare frequency, the variation of the amplitude and shape of the light-curve structures for AU Mic and YZ CMi in two years, the

model selection for each number of spots, and the validity of starspot modeling.

In Section 3, we described the main results, summarized as follows:

1. The flare frequency is not necessarily correlated with the rotation phase of the light curve for each star. We suggest that this can be because any spot is always visible in all phases for any model due to multiple spots or a moderate inclination angle for each star. As a result, flares can be distributed in all rotation phases.

2. For AU Mic and YZ CMi, the amplitude and shape of the light curve have varied in two years, whereas the flare frequency is almost constant within an error. The result of

starspot modeling suggests that the variation of the light curve can be explained by the variations of spot size and latitude. We also find that the total spot area does not change significantly enough in two years to change the flare frequency within the error, and this is why the flare frequency does not vary in two years.

EV Lac was observed in Sectors 56 and 57 (September 1 to October 29 in 2022) through the TESS second extended mission (Cycle 5). Then, the three-year variation of the light curve can be investigated as in Section 3.3. In future studies, it will be necessary to conduct surface mapping in multiband wavelengths (e.g., Morris et al. 2018; Namekata et al. 2020; Toriumi et al. 2020), taking into account the effects of bright spots (faculae) and constraints on the spot temperature (e.g., Johnson et al. 2021). It will also be helpful to scan the stellar surface for spot occultations by multiple transits of exoplanets (e.g., Morris et al. 2017; Namekata et al. 2020; Bruno & Deleuil 2021). Surface mapping on the stellar surface plays an important role in quantifying stellar effects on exoplanet characterizations (Rackham et al. 2018, 2023).

Appendix A
Other Models with Different Assumptions

To evaluate the uncertainties of the parameters (Section 2.2), we also perform starspot modeling with the two-spot model for the light curve of EV Lac Cycle 2 with different assumptions: the quadratic limb-darkening law in Section A.1, parameters including the spot relative intensity under uniform and normal prior distributions in Section A.2, and the two-spot model with systematic noise by a GP in Section A.3. The deduced parameters are listed in Table A1.

A.1. Quadratic Limb-darkening Law

To compare the result by the quadratic limb-darkening law with that by the nonlinear law (Table 1), we also fix the coefficient values $c_1 = c_3 = 0$, $c_2 = u_1 + 2u_2 = 1.04$, and $c_4 = -u_2 = -0.44$ in Equation (4), where $u_1 = 0.16$ and $u_2 = 0.44$ (Equation (17) in Paper I) from Claret (2018). As a result, the uncertainties of the

spot parameters are of the same degree as those in the two-spot model (Table 6). The uncertainties of the stellar parameters increase by an order of magnitude, but remain small. The deduced latitude of the second spot is lower because there are degeneracies between the spot latitude and size due to the high inclination angle $= 60$ (deg) (Paper I).

A.2. Spot Relative Intensity with Uniform and Normal Prior Distributions

To take account of the degeneracies between spot latitude and spot relative intensity, we also include them as parameters under uniform and normal prior distributions extended to the range of 0 to 2 for bright spots as reported in Morris et al. (2018). As a result, the uncertainties of the stellar parameters are also of the same degree as those in the two-spot model (Table 6). The uncertainties of the spot parameters increase by a factor, but remain small. The deduced latitude of the second spot is lower for the same reason mentioned in Section A.1, and the deduced radii are larger because the deduced relative intensity is higher (Section 2.2). The deduced spot intensities $f_{\rm spot} = 0.833$ and 0.811 for the uniform and normal prior distributions correspond to spot temperatures $T_{\rm spot} = 3284$ and 3268 (K), respectively (Equation (3)).

A.3. Two-spot and Systematic Noise Models

To evaluate systematic noise in the residual from the two-spot model, we simultaneously perform modeling of the noise with a GP (Foreman-Mackey et al. 2017; Günther & Daylan 2021). Then, we employ a multivariate normal likelihood function with the Matérn 3/2 kernel characterized by hyperparameters $\sigma_{\rm sys}$ and $\rho_{\rm sys}$:

$$p(\mathcal{D}|\theta) = \frac{1}{(\sqrt{2\pi})^N \sqrt{|\boldsymbol{K} + \sigma_i^2 \boldsymbol{I}|}} \times$$

$$\exp\left[-\frac{1}{2}(\boldsymbol{F}_{\rm obs} - \boldsymbol{F}_{\rm mod}(\theta))^{\rm T} (\boldsymbol{K} + \sigma_i^2 \boldsymbol{I})^{-1}(\boldsymbol{F}_{\rm obs} - \boldsymbol{F}_{\rm mod}(\theta)) \right]$$

$$(A1)$$

and

$$K(t_i, t_j) = \sigma_{\rm sys}^2 \left(1 + \frac{\sqrt{3}\,|t_i - t_j|}{\rho_{\rm sys}} \right) \exp\left(-\frac{\sqrt{3}\,|t_i - t_j|}{\rho_{\rm sys}} \right),$$

$$(A2)$$

where θ, $\mathcal{D}$, σ_i, $\boldsymbol{F}_{\rm obs}$, and $\boldsymbol{F}_{\rm mod}$ denote the parameters, the observed data, the photometric error, the vector of the observed flux, and the vector of the model flux, respectively. As a result, the uncertainties of the spot parameters are slightly larger than those in the two-spot model (Table 6) up to an order of magnitude because the systematic noise model enables us to optimize the residual from the spot model flexibly. The uncertainties of the stellar parameters increase by 2 orders of magnitude, but remain small. The deduced latitude of the second spot is also lower for the same reason mentioned in Section A.1.

Table A1
EV Lac Cycle 2 Additional Cases

Deduced Parameters	Quadratic Limb Darkening	Uniform	Normal	GP	Prior Distribution[a]
(Stellar parameters)					
1. Equatorial period $P_{\rm eq}$ (day)	$4.3482^{+0.0007}_{-0.0010}$	$4.3554^{+0.0002}_{-0.0004}$	$4.3559^{+0.0003}_{-0.0003}$	$4.3518^{+0.0019}_{-0.0106}$	$\mathcal{U}_{\rm log}(4.0000, 5.0000)$
2. Degree of differential rotation κ	$0.0147^{+0.0011}_{-0.0010}$	$0.0037^{+0.0003}_{-0.0002}$	$0.0032^{+0.0002}_{-0.0001}$	$0.0120^{+0.0129}_{-0.0026}$	$\mathcal{U}(-0.2000, 0.2000)$
(Spot parameters)					
(First spot)					
3. Latitude Φ_1 (deg)	$22.59^{+0.24}_{-0.20}$	$25.70^{+0.31}_{-0.39}$	$25.41^{+0.38}_{-0.33}$	$21.11^{+1.92}_{-1.52}$	$\mathcal{U}(-90.00, \Phi_2)$[b]
4. Initial longitude Λ_1 (deg)	$50.30^{+0.13}_{-0.10}$	$56.56^{+0.27}_{-0.20}$	$57.28^{+0.22}_{-0.20}$	$50.30^{+0.73}_{-0.71}$	$\mathcal{U}(-180.00, 180.00)$
5. Maximum radius $\alpha_{\rm max,1}$ (deg)	$12.41^{+0.01}_{-0.01}$	$24.35^{+0.21}_{-0.17}$	$22.78^{+0.20}_{-0.19}$	$12.46^{+0.05}_{-0.04}$	$\mathcal{U}(0.01, 30.00)$
(Second spot)					
6. Latitude Φ_2 (deg)	$30.29^{+0.33}_{-0.26}$	$46.14^{+0.65}_{-0.60}$	$48.06^{+0.67}_{-0.47}$	$29.16^{+1.64}_{-1.89}$	$\mathcal{U}(\Phi_1, 90.00)$[b]
7. Initial longitude Λ_2 (deg)	$-85.66^{+0.09}_{-0.12}$	$-86.97^{+0.17}_{-0.14}$	$-86.44^{+0.17}_{-0.14}$	$-85.56^{+0.79}_{-0.72}$	$\mathcal{U}(-180.00, 180.00)$
8. Maximum radius $\alpha_{\rm max,2}$ (deg)	$11.77^{+0.01}_{-0.01}$	$24.48^{+0.21}_{-0.21}$	$23.14^{+0.22}_{-0.22}$	$11.78^{+0.06}_{-0.04}$	$\mathcal{U}(0.01, 30.00)$
(Additional parameters)					
9. Relative intensity $f_{\rm spot}$	0.48 (fixed)	$0.833^{+0.002}_{-0.002}$	$0.811^{+0.003}_{-0.003}$	0.48 (fixed)	$\mathcal{U}(0.00, 2.00)$ / $\mathcal{TN}(0.48, 0.01, 0.00, 2.00)$
10. GP amplitude $\log \sigma_{\rm sys}$	⋯	⋯	⋯	$-6.5994^{+0.0181}_{-0.0130}$	$\mathcal{U}(-10.0, 0.0)$
11. GP exponential length $\log \rho_{\rm sys}$	⋯	⋯	⋯	$-5.1250^{+0.0235}_{-0.0198}$	$\mathcal{U}(-10.0, 0.0)$
Average flux $F_{\rm ave}$	0.854	0.851	0.851	0.856	
Logarithm of model evidence $\log \mathcal{Z}$	−5995.666	−5654.106	−5753.989	21,813.240	

Notes.

[a] $\mathcal{U}_{\rm log}(a, b) = 1/(\theta \log(b/a))$, $\mathcal{U}(a, b) = 1/(b-a)$, and $\mathcal{TN}(\mu, \sigma^2, a, b)$ represent the bounded log uniform distribution (Jeffreys prior), bounded uniform distribution, and truncated normal distribution defined in $a \leqslant \theta \leqslant b$, respectively.

[b] We discern each spot by its latitude Φ_k, not by its reference time t_k as in Paper I, to improve the sampling efficiency of the PT.

Appendix B
Joint Posterior Distributions

The joint posterior distributions of the equatorial period P_{eq}, degree of differential rotation κ, latitude Φ_k, initial longitude Λ_k, and maximum radius $\alpha_{max,k}$ are delineated in Figures B1, B2, B3, B4, B5, B6, B7, B8, B9, and B10 for AU Mic Cycles 1 and 3, YZ CMi Cycles 1 and 3, and EV Lac Cycle 2, generated with corner (Foreman-Mackey 2016). All figures show each of the distributions is a unimodal distribution.
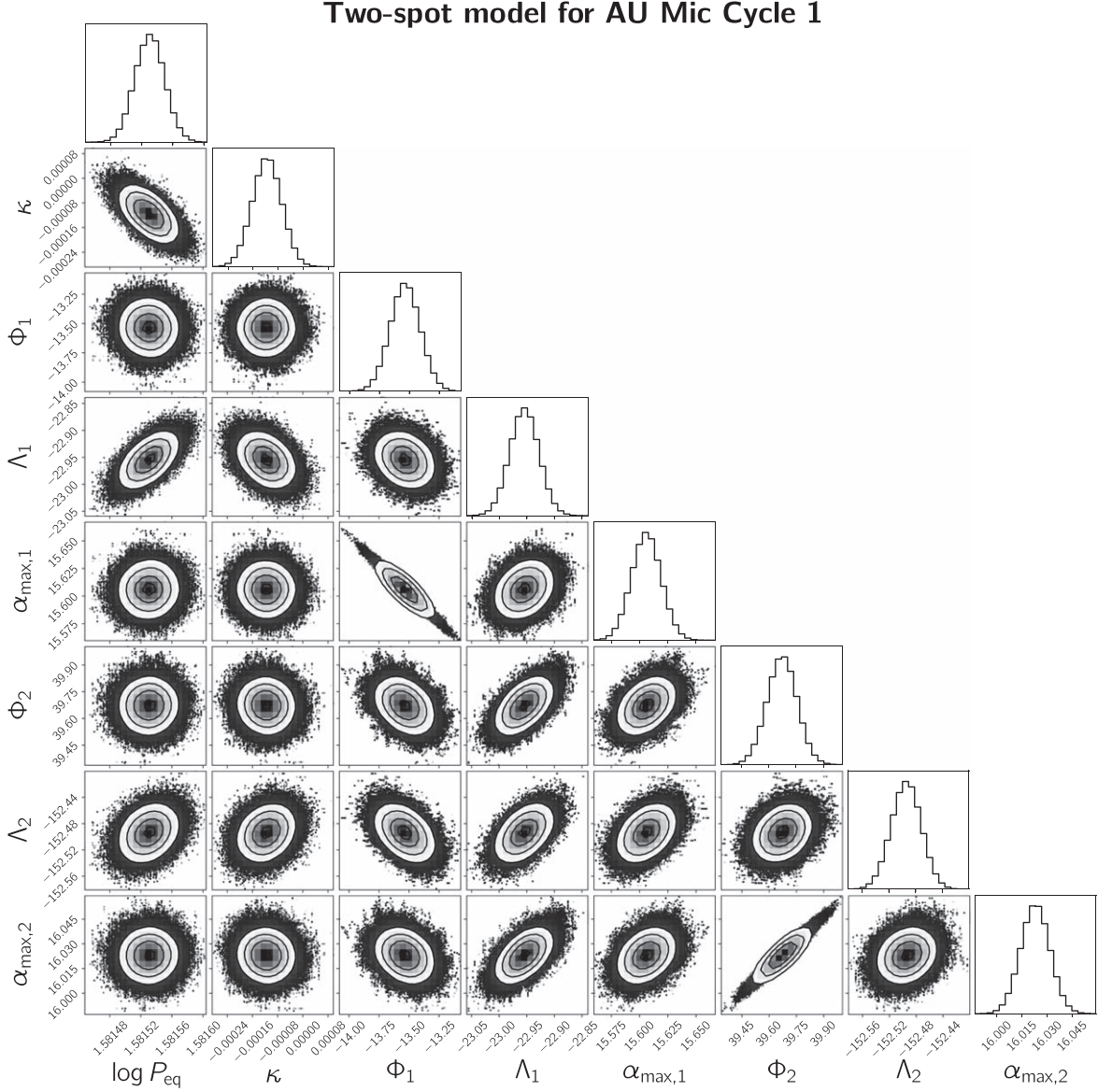

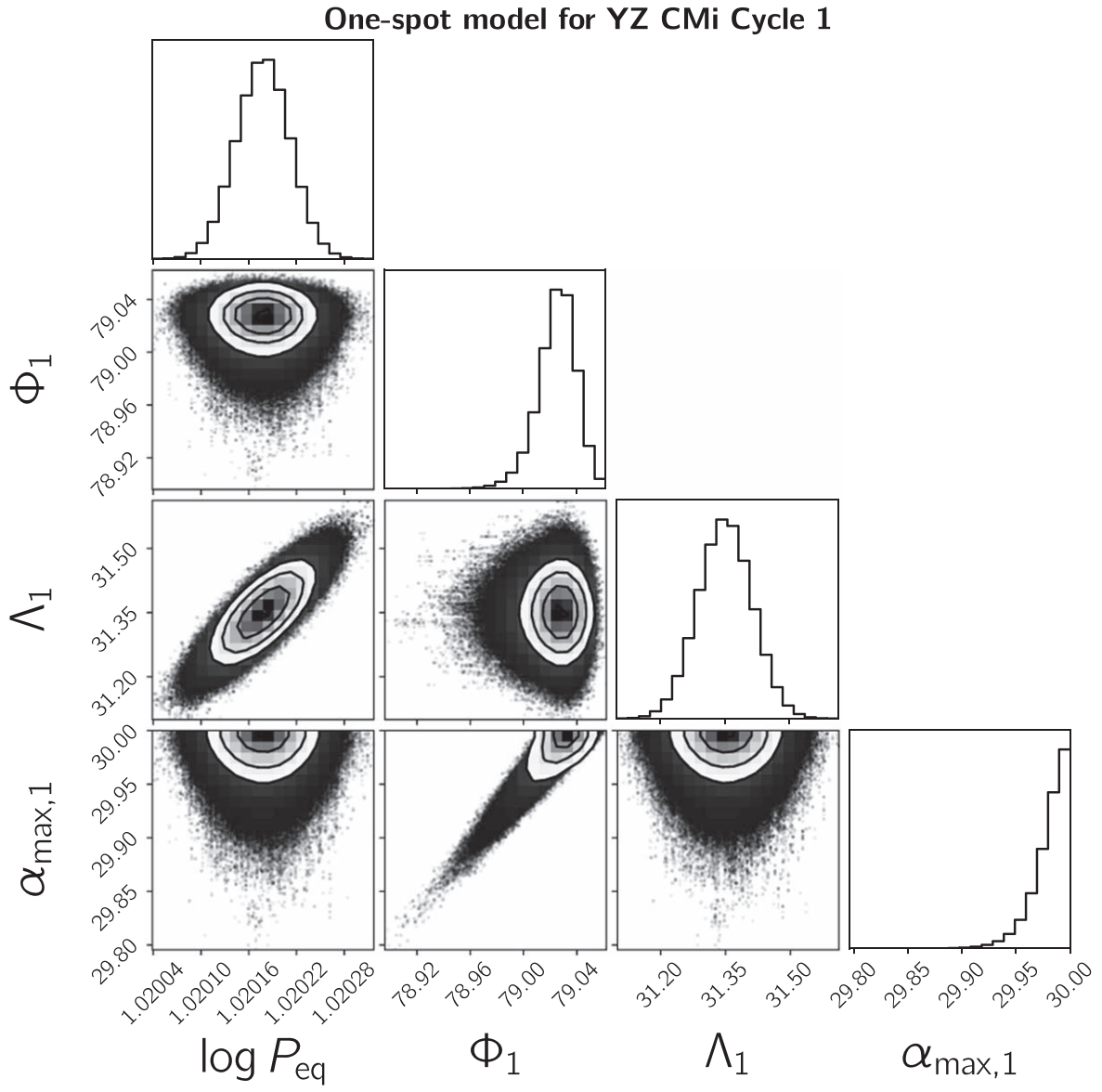
Two-spot model for AU Mic Cycle 1

Figure B1. The joint posterior distribution of parameters for the light curve of AU Mic Cycle 1 with the two-spot model. Each column represents the equatorial period P_{eq}, degree of differential rotation κ, latitude Φ_k, initial longitude Λ_k, or maximum radius $\alpha_{max,k}$.

Three-spot model for AU Mic Cycle 1
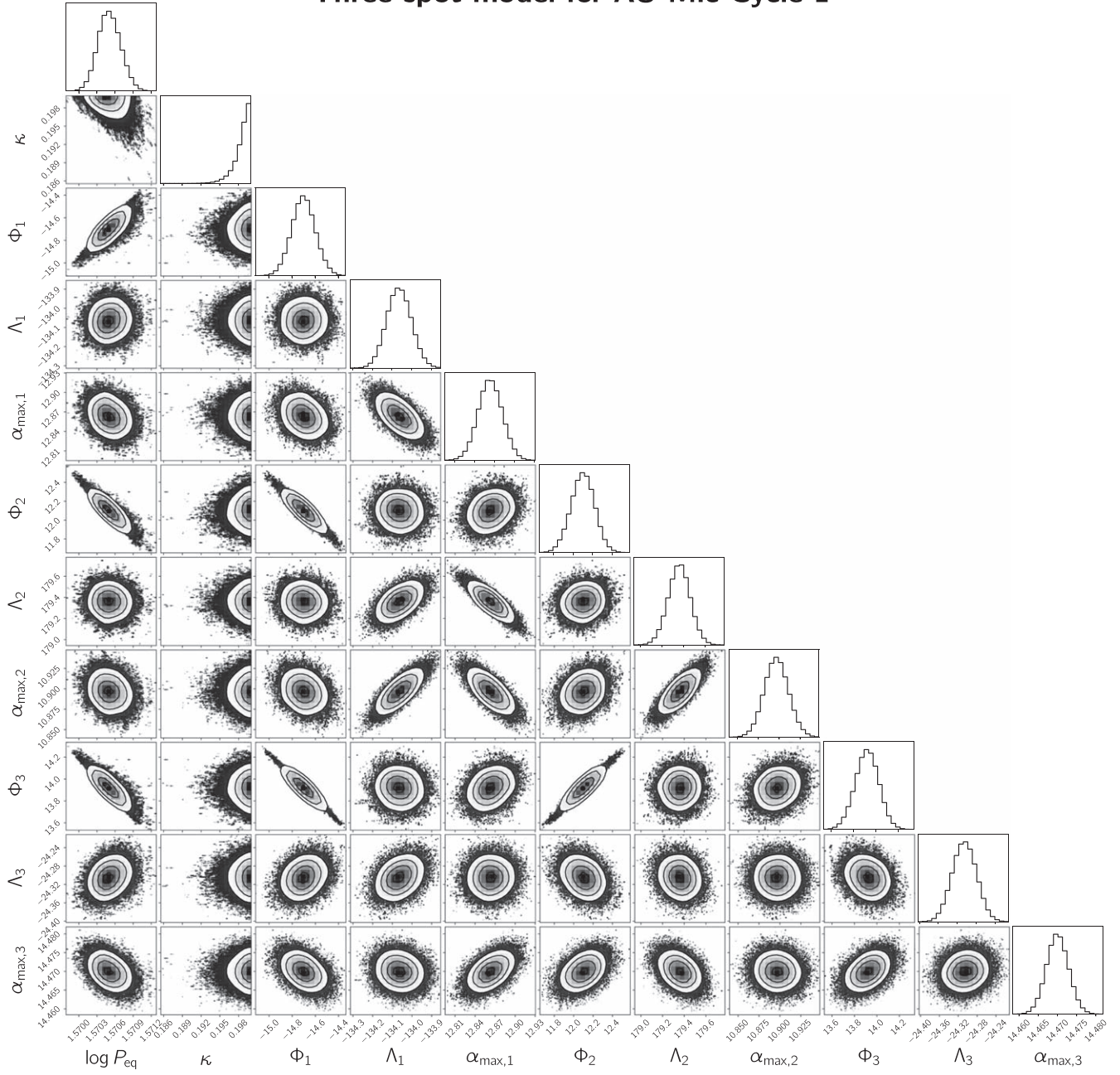
Figure B2. Same as Figure B1 but for the three-spot model.
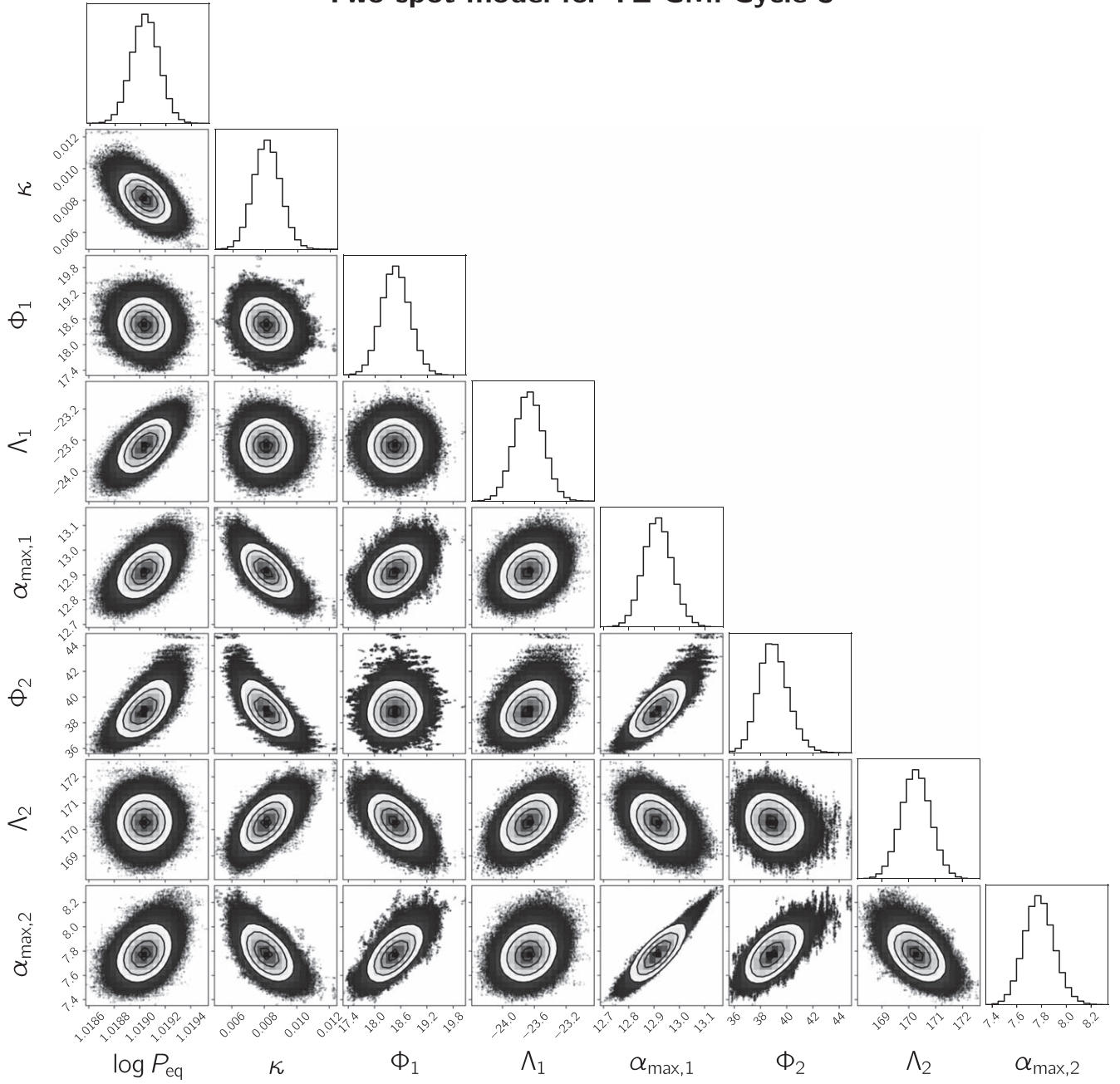
Two-spot model for AU Mic Cycle 3
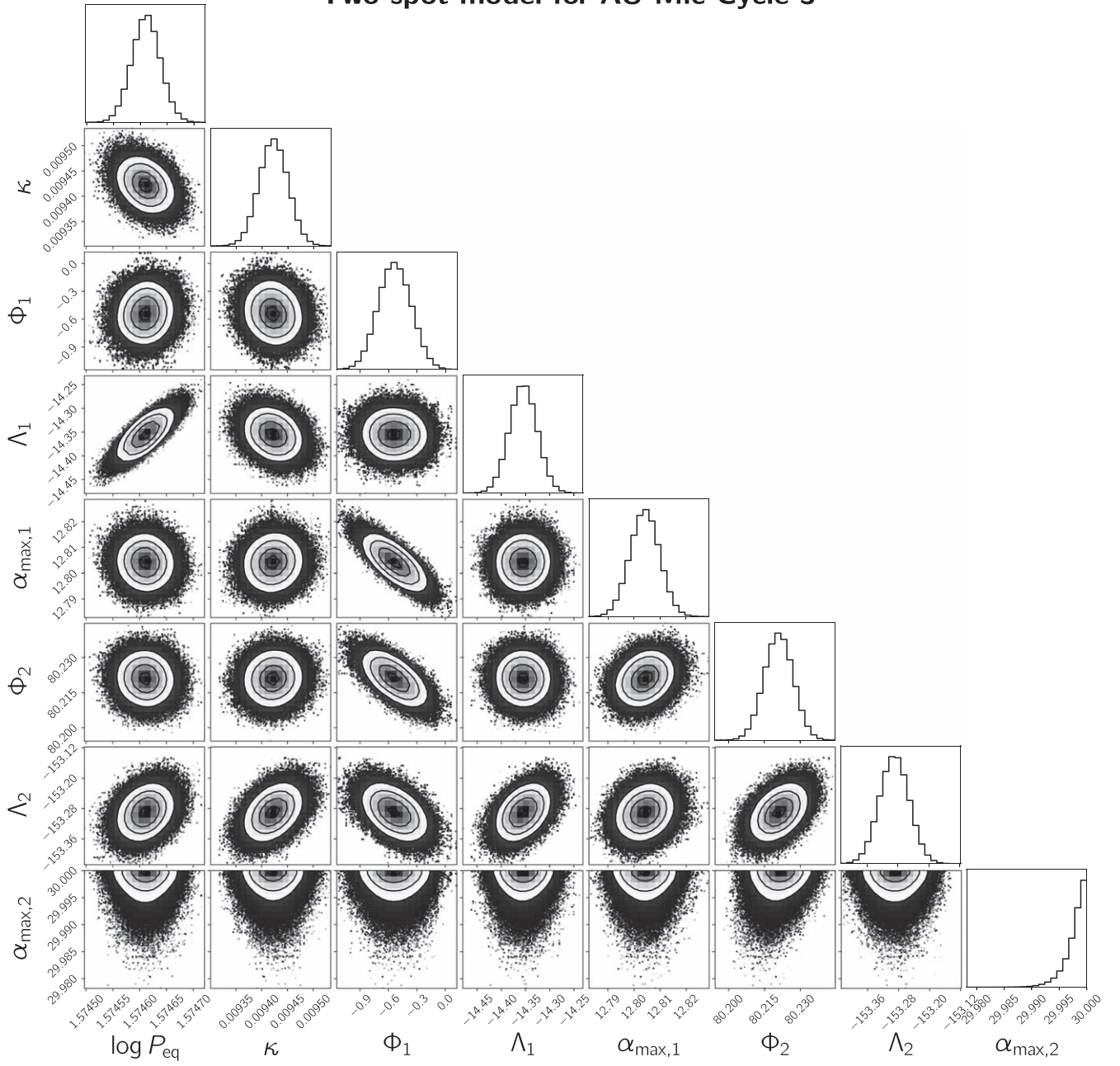
Figure B3. Same as Figure B1 but for AU Mic Cycle 3.
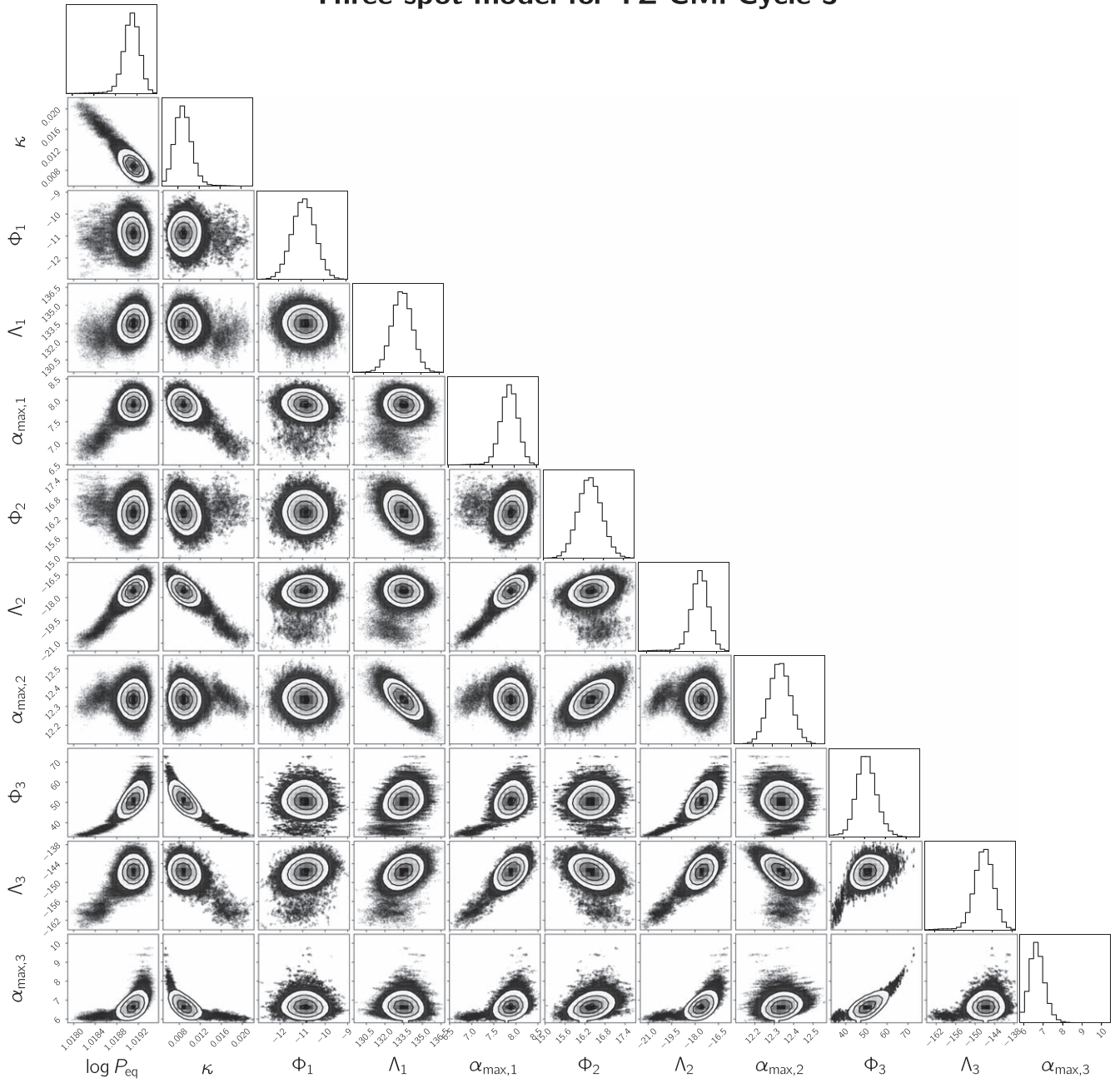
Three-spot model for AU Mic Cycle 3
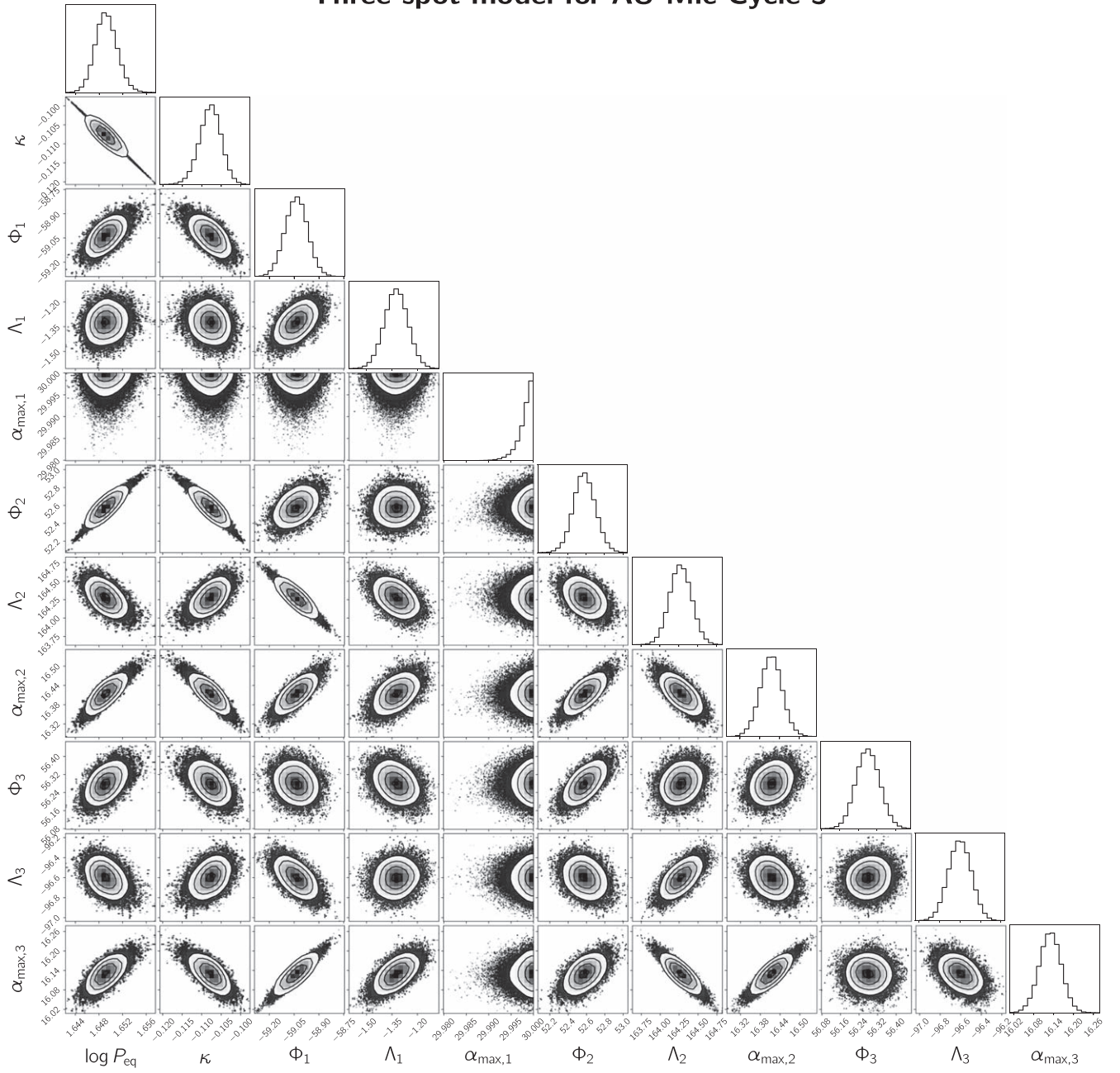
Figure B4. Same as Figure B3 but for the three-spot model.
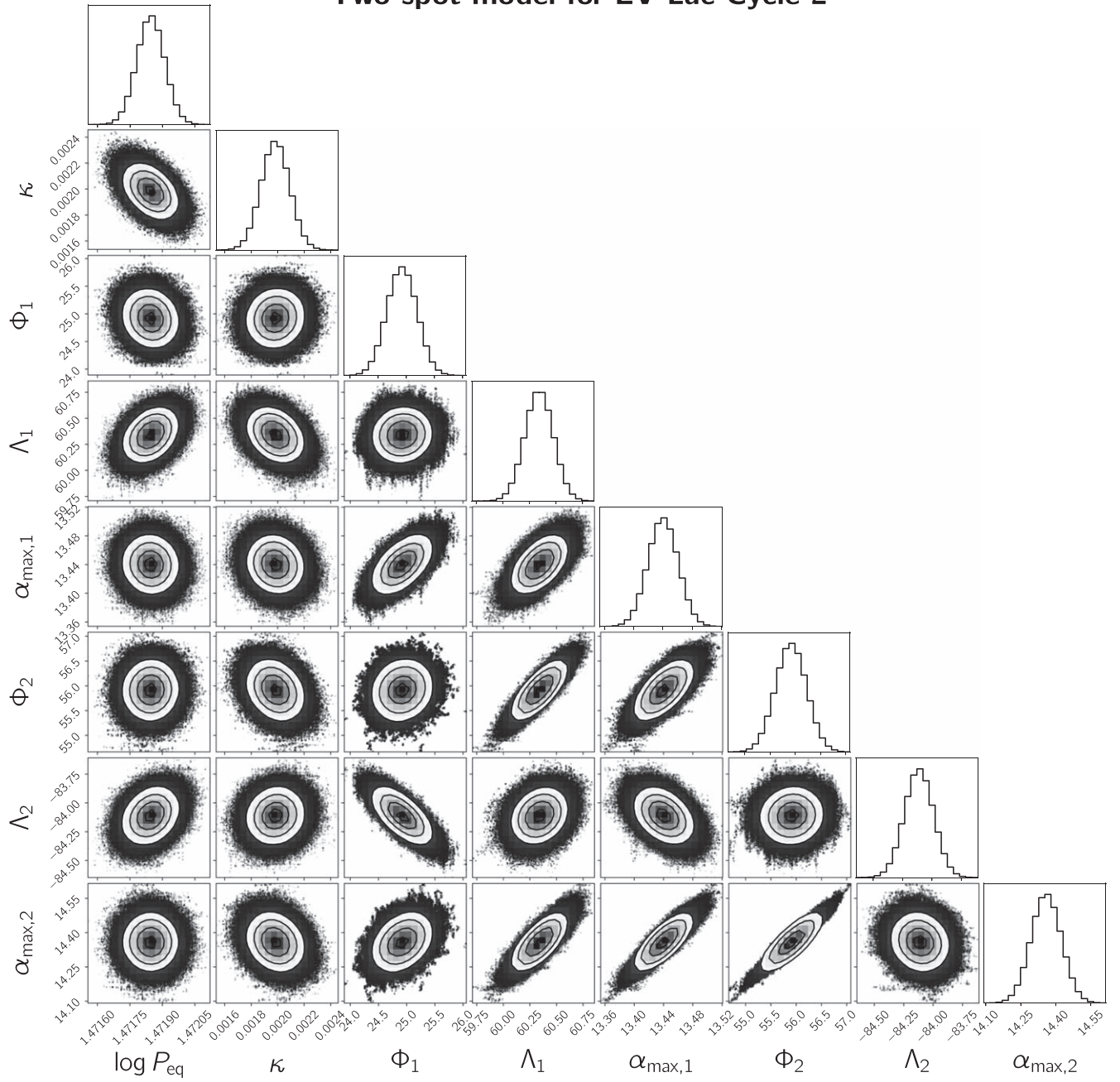
Two-spot model for YZ CMi Cycle 1
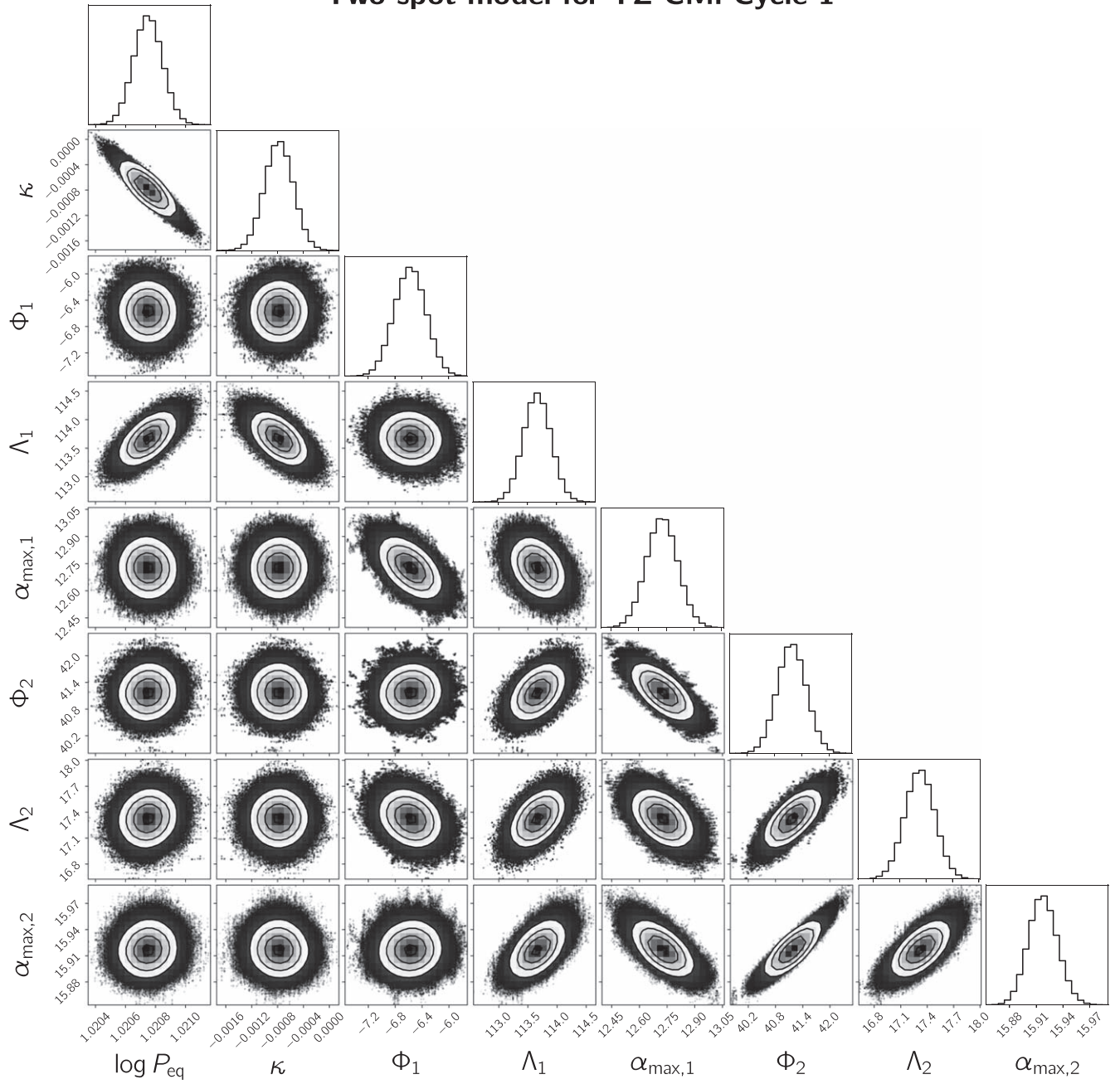
Figure B5. The joint posterior distribution of parameters for the light curve of YZ CMi Cycle 1 with the two-spot model. Each column represents the equatorial period P_{eq}, degree of differential rotation κ, latitude Φ_k, initial longitude Λ_k, or maximum radius $\alpha_{max,k}$.

One-spot model for YZ CMi Cycle 1

Figure B6. Same as Figure B5 but for the one-spot model.

Two-spot model for YZ CMi Cycle 3

Figure B7. Same as Figure B5 but for YZ CMi Cycle 3.

Three-spot model for YZ CMi Cycle 3

Figure B8. Same as Figure B7 but for the three-spot model.

Two-spot model for EV Lac Cycle 2

Figure B9. The joint posterior distribution of parameters for the light curve of EV Lac Cycle 2 with the two-spot model. Each column represents the equatorial period $P_{\rm eq}$, degree of differential rotation κ, latitude Φ_k, initial longitude Λ_k, or maximum radius $\alpha_{{\rm max},k}$.

Three-spot model for EV Lac Cycle 2
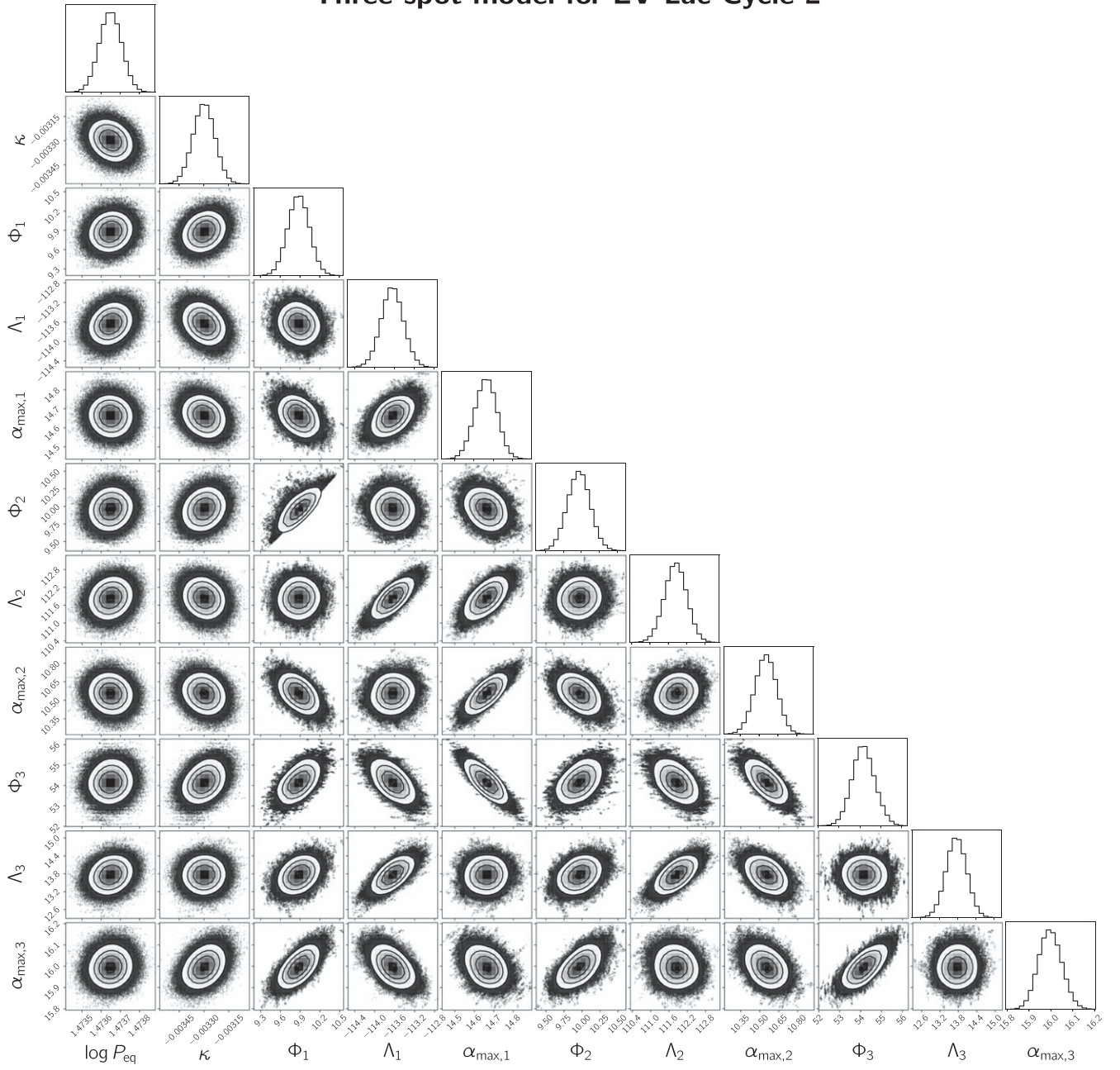
Figure B10. Same as Figure B9 but for the three-spot model.

ORCID iDs

Kai Ikuta ⓘ https://orcid.org/0000-0002-5978-057X
Kosuke Namekata ⓘ https://orcid.org/0000-0002-1297-9485
Yuta Notsu ⓘ https://orcid.org/0000-0002-0412-0849
Hiroyuki Maehara ⓘ https://orcid.org/0000-0003-0332-0811
Satoshi Honda ⓘ https://orcid.org/0000-0001-6653-8741
Daisaku Nogami ⓘ https://orcid.org/0000-0001-9588-1872
Kazunari Shibata ⓘ https://orcid.org/0000-0003-1206-7889

References

Basri, G., & Nguyen, H. T. 2018, ApJ, 863, 190
Baroch, D., Morales, J. C., Ribas, I., et al. 2020, A&A, 641, A69
Basri, G. 2018, ApJ, 865, 142
Basri, G., & Shah, R. 2020, ApJ, 901, 14
Benz, A. O., & Güdel, M. 2010, ARA&A, 48, 241
Berdyugina, S. V. 2005, LRSP, 2, 8
Bicz, K., Falewicz, R., Pietras, M., et al. 2022, ApJ, 935, 102
Bruno, G., & Deleuil, M. 2021, arXiv:2104.06173
Butler, C. J., Doyle, J. G., Andrews, A. D., et al. 1987, A&A, 174, 139
Cifuentes, C., Caballero, J. A., Cortés-Contreras, M., et al. 2020, A&A, 642, A115
Claret, A. 2018, A&A, 618, A20
Davenport, J. R. A., Hawley, S. L., Hebb, L., et al. 2014, ApJ, 797, 122
Davenport, J. R. A., Hebb, L., & Hawley, S. L. 2015, ApJ, 806, 212
Doyle, L., Ramsay, G., Doyle, J. G., et al. 2018, MNRAS, 480, 2153
Doyle, L., Ramsay, G., & Doyle, J. G. 2020, MNRAS, 494, 3596
Feinstein, A., Montet, B., & Ansdell, M. 2020, JOSS, 5, 2347
Feinstein, A. D., Montet, B. T., Ansdell, M., et al. 2020, AJ, 160, 219
Feinstein, A. D., Seligman, D. Z., Günther, M. N., et al. 2022, ApJL, 925, L9
Foreman-Mackey, D. 2016, JOSS, 1, 24
Foreman-Mackey, D., Agol, E., Ambikasaran, S., et al. 2017, AJ, 154, 220
Gelman, A., Carlin, J. B., Stern, H. S., & Rubin, D. B. 1995, Bayesian Data Analysis (New York: Chapman & Hall),
Gershberg, R. E. 2005, Solar-Type Activity in Main-Sequence Stars (Berlin: Springer)
Gilbert, E. A., Barclay, T., Quintana, E. V., et al. 2022, AJ, 163, 147
Grindlay, J., & Heise, J. 1975, ICRC, 1, 154
Günther, M. N., & Daylan, T. 2021, ApJS, 254, 13
Günther, M. N., Zhan, Z., Seager, S., et al. 2020, AJ, 159, 60
Hawley, S. L., Davenport, J. R. A., Kowalski, A. F., et al. 2014, ApJ, 797, 121
Hawley, S. L., & Pettersen, B. R. 1991, ApJ, 378, 725
Hebb, L., Petro, L., Ford, H. C., et al. 2007, MNRAS, 379, 63
Hedges, C., Angus, R., Barentsen, G., et al. 2020, RNAAS, 4, 220
Henry, G. W., Eaton, J. A., Hamer, J., et al. 1995, ApJS, 97, 513
Herbst, K., Papaioannou, A., Airapetian, V. S., et al. 2021, ApJ, 907, 89
Honda, S., Notsu, Y., Namekata, K., et al. 2018, PASJ, 70, 62
Hukushima, K. 1999, PhRvE, 60, 3606
Ikuta, K., Maehara, H., Notsu, Y., et al. 2020, ApJ, 902, 73, (Paper I)
Jeffers, S. V., Barnes, J. R., Schöfer, P., et al. 2022, A&A, 663, A27
Johnson, L. J., Norris, C. M., Unruh, Y. C., et al. 2021, MNRAS, 504, 4751
Kalas, P., Liu, M. C., & Matthews, B. C. 2004, Sci, 303, 1990
Karoff, C., Knudsen, M. F., De Cat, P., et al. 2016, NatCo, 7, 11058
Kass, R. E., & Raftery, A. E. 1995, J. Am. Stat. Assoc., 90, 773
Kipping, D. M. 2012, MNRAS, 427, 2487

Klein, B., Donati, J.-F., Moutou, C., et al. 2021, MNRAS, 502, 188
Klein, B., Zicher, N., Kavanagh, R. D., et al. 2022, MNRAS, 512, 5067
Koch, D. G., Borucki, W. J., Basri, G., et al. 2010, ApJL, 713, L79
Kochukhov, O. 2021, A&ARv, 29, 1
Kowalski, A. F., Hawley, S. L., Holtzman, J. A., et al. 2010, ApJL, 714, L98
Kundu, M. R., Jackson, P. D., White, S. M., et al. 1987, ApJ, 312, 822
Kunkel, W. E. 1970, PASP, 82, 1341
Lacy, C. H., Moffett, T. J., & Evans, D. S. 1976, ApJS, 30, 85
Luger, R., Bedell, M., Foreman-Mackey, D., et al. 2021, arXiv:2110.06271
Luger, R., Foreman-Mackey, D., Hedges, C., et al. 2021a, AJ, 162, 123
Luger, R., Foreman-Mackey, D., & Hedges, C. 2021b, AJ, 162, 124
Maehara, H., Notsu, Y., Namekata, K., et al. 2021, PASJ, 73, 44
Maehara, H., Notsu, Y., Notsu, S., et al. 2017, PASJ, 69, 41
Maehara, H., Shibayama, T., Notsu, S., et al. 2012, Natur, 485, 478
Martioli, E., Hébrard, G., Moutou, C., et al. 2020, A&A, 641, L1
Messina, S., & Guinan, E. F. 2002, A&A, 393, 225
Mitra-Kraev, U., Harra, L. K., Güdel, M., et al. 2005, A&A, 431, 679
Morin, J., Donati, J.-F., Petit, P., et al. 2008, MNRAS, 390, 567
Morris, B. M., Agol, E., Davenport, J. R. A., et al. 2018, ApJ, 857, 39
Morris, B. M., Hebb, L., Davenport, J. R. A., et al. 2017, ApJ, 846, 99
Muheki, P., Guenther, E. W., Mutabazi, T., et al. 2020, MNRAS, 499, 5047
Namekata, K., Davenport, J. R. A., Morris, B. M., et al. 2020, ApJ, 891, 103
Namekata, K., Maehara, H., Honda, S., et al. 2021, NatAs, 6, 241
Namekata, K., Maehara, H., Honda, S., et al. 2022, ApJL, 926, L5
Namekata, K., Maehara, H., Sasaki, R., et al. 2020, PASJ, 72, 68
Notsu, Y., Maehara, H., Honda, S., et al. 2019, ApJ, 876, 58
Notsu, Y., Shibayama, T., Maehara, H., et al. 2013, ApJ, 771, 127
Okamoto, S., Notsu, Y., Maehara, H., et al. 2021, ApJ, 906, 72
Osten, R. A., Hawley, S. L., Allred, J. C., et al. 2005, ApJ, 621, 398
Paudel, R. R., Barclay, T., Schlieder, J. E., et al. 2021, ApJ, 922, 31
Pettersen, B. R. 1980, AJ, 85, 871
Pettersen, B. R., Kern, G. A., & Evans, D. S. 1983, A&A, 123, 184
Plavchan, P., Barclay, T., Gagné, J., et al. 2020, Natur, 582, 497
Rackham, B. V., Apai, D., & Giampapa, M. S. 2018, ApJ, 853, 122
Rackham, B. V., Espinoza, N., Berdyugina, S. V., et al. 2023, RASTI, 2, 148
Ricker, G. R., Winn, J. N., Vanderspek, R., et al. 2015, JATIS, 1, 014003
Rodono, M., Cutispoto, G., Pazzani, V., et al. 1986, A&A, 165, 135
Roettenbacher, R. M., Monnier, J. D., Korhonen, H., et al. 2017, ApJ, 849, 120
Rojas-Ayala, B., Covey, K. R., Muirhead, P. S., et al. 2012, ApJ, 748, 93
Shibata, K., Isobe, H., Hillier, A., et al. 2013, PASJ, 65, 49
Shibayama, T., Maehara, H., Notsu, S., et al. 2013, ApJS, 209, 5
Silverberg, S. M., Kowalski, A. F., Davenport, J. R. A., et al. 2016, ApJ, 829, 129
Spangler, S. R., Shawhan, S. D., & Rankin, J. M. 1974, ApJL, 190, L129
Strassmeier, K. G. 2009, A&ARv, 17, 251
Strassmeier, K. G., & Bopp, B. W. 1992, A&A, 259, 183
Strassmeier, K. G., Lupinek, S., Dempsey, R. C., et al. 1999, A&A, 347, 212
Toriumi, S., Airapetian, V. S., Hudson, H. S., et al. 2020, ApJ, 902, 36
Torres, C. A. O., Ferraz Mello, S., & Quast, G. R. 1972, ApL, 11, 13
Tu, Z.-L., Yang, M., Wang, H.-F., et al. 2021, ApJS, 253, 35
Tu, Z.-L., Yang, M., Zhang, Z. J., et al. 2020, ApJ, 890, 46
Vousden, W. D., Farr, W. M., & Mandel, I. 2016, MNRAS, 455, 1919
Walkowicz, L. M., Basri, G., & Valenti, J. A. 2013, ApJS, 205, 17
Wisniewski, J. P., Kowalski, A. F., Davenport, J. R. A., et al. 2019, ApJL, 883, L8
Zboril, M. 2003, AN, 324, 527